Computer Methods in Applied Mechanics and Engineering 448 (2026) 118452

Contents lists available at ScienceDirect

Comput. Methods Appl. Mech. Engrg.

journal homepage: www.elsevier.com/locate/cma

A novel data-driven surrogate approach for fast evaluation of the dynamics of soft ellipsoidal micro-particles in dilute viscous flow

Jana Wedel [a,*], Ivan Dominik Horvat [b], Nejc Vovk [b], Matjaž Hriberšek [b], Jure Ravnik [b], Paul Steinmann [a,c]

[a] Institute of Applied Mechanics, Friedrich-Alexander-Universität Erlangen-Nürnberg, Germany
[b] Faculty of Mechanical Engineering, University of Maribor, Slovenia
[c] Glasgow Computational Engineering Center, University of Glasgow, United Kingdom

ARTICLE INFO

Keywords:
Neural network
Pseudo-rigid bodies
Barycenter and shape dynamics
Lagrangian particle tracking

ABSTRACT

We present a novel data-driven surrogate approach for fast evaluation of the deformation dynamics of soft particles, both initially spherical and ellipsoidal, suspended in external flows, specifically predicting the hydrodynamic tractions on the particle surface. The core of the approach relies on expressing the required force dyad as a linear combination of velocity gradient components, modulated by form coefficients. These coefficients scale shear, rotational, and extensional flow contributions to the velocity gradient. Two training strategies are proposed: one utilizing analytical data, which enables a computational speedup, and another based on data obtained with 3D direct numerical simulations (DNS) using the boundary element method (BEM), with the latter demonstrating the feasibility of this approach even in the absence of analytical solutions. Validation against established literature benchmarks confirms the model's accuracy in three scenarios: (i) ellipsoidal particles in the quasi-rigid limit in pipe flow, (ii) initially spherical particles in shear flow, and (iii) initially ellipsoidal particles in shear flow. In all cases, the data-driven surrogate approach achieves excellent agreement with reference results. This work establishes a foundation for extending our data-driven approach to flow-induced deformations of soft particles of more complex particle shapes, such as superellipsoids and other non-ellipsoidal geometries, where no analytical traction expression is available.

1. Introduction

Particles suspended in flows are ubiquitous in both natural and industrial (petrochemical, wastewater, cement, or pharmaceutical industries, [1,2]) contexts, ranging from biological entities (platelets in blood, pollen, sand) to environmental pollutants such as microplastics and tire wear. The study of rigid spherical and non-spherical particle suspensions has garnered extensive attention, with a rich body of analytical [3–7], experimental [8–12], and computational [13–20] research over the last century. However, the dynamics of soft particles suspended in flows, which can deform due to the fluid-flow-induced tractions exerted on the particle surface, remain less explored despite their significant presence in both engineered and natural systems. Examples of soft particles include man-made entities such as liposomes and hydrogels (gaining significant importance in the medical field), as well as naturally occurring biological cells and microorganisms (bacteria, algae). The limited research on soft particles, particularly in scenarios involving large particle populations, has resulted in a gap in our understanding of these complex systems.

* Corresponding author.
E-mail address: jana.wedel@fau.de (J. Wedel).

https://doi.org/10.1016/j.cma.2025.118452

Available online 30 October 2025

1.1. State-of-the-art

Fröhlich and Sack conducted some of the first investigations on soft initially spherical particles [21], where they examined Hookean elastic particles in extensional flows. Subsequent studies, such as those by Cerf [22] and Goddard & Miller [23], studied soft initially spherical particles with viscoelastic material behaviour in various flow conditions. In particular, Roscoe [24] was the first to explore suspensions of viscoelastic micro-particles under conditions of finite deformation, extending the foundational work of Jeffery [7], who studied rigid ellipsoidal particles. Roscoe's findings indicated that soft initially spherical particles in shear flow evolve through a series of ellipsoidal shapes to a steady-state ellipsoidal shape with a steady-state orientation. Nevertheless, the material exhibits continuous deformation – a phenomenon known as tank-treading, [24,25]. The underlying assumption of affine deformation was later validated through numerical simulations by Gao & Hue [25] and Gao et al. [26], who employed a discretized particle method (ALE-FEM) and confirmed the predicted steady-state shapes and orientations of soft initially spherical particles in simple shear flow.

In later studies, Gao et al. [27] investigated soft initially ellipsoidal particles and observed two distinct dynamics regimes, i.e., tumbling (TU) and trembling (TR), which depend on the initial (i.e., stress-free) shape of the ellipsoid. These dynamical regimes are also experimentally observable for example in the case of vesicles [27]. In a later work, Gao et al. [28] studied initially elliptic particles (two-dimensional) in extensional flow and found that their steady-state shape (characterized by alignment of the particle's long axis with the extensional flow direction) differs from that of a similar particle in shear flow.

In the work of Sanagavarapu et al., [29] the authors pointed out that the theoretical framework of Gao et al. [25–28] is limited as it is based on the upper convective time derivative of the Neo-Hooke constitutive relation to obtain the relation between stress and strain rate and is thus not applicable for more general constitutive models (such as the Mooney-Rivlin constitutive model) as the stress-rate might not solely depend on the strain rate. Consequently, the authors advocate rather to employing a relation between total stress and total strain [29].

To summarize, the computational approaches available in the literature have primarily focused on initially spherical or ellipsoidal soft particles under restrictive assumptions, which limit their applicability to more complex scenarios [30]. For example,the frameworks developed by Gao et al. [25–28] and Sanagavarapu et al. [29] require (surface and volume) discretization, imposing significant computational costs when studying large numbers of soft particles.

Recent advancements were presented in our previous work, see Wedel et al., [30] for soft initially spherical particles and [31] for the extension to soft initially ellipsoid particles. In these works, we proposed a novel deformable particle approach that allows efficient tracking of large populations of soft particles in arbitrary (global) flow conditions. This model leverages the pseudo-rigid body theory [32] in combination with affine deformations and Lagrangian point-particle tracking, facilitating the study of the dynamics of soft initially spherical and ellipsoidal particles without the computational burden associated with the state-of-the-art methods that rely on particle surface (and volume) discretization.

As presented, the novel approach excellently replicates the behavior of soft initially spherical [25,26] as well as initially ellipsoidal [27,29] particles as reported in the literature, however, at significantly reduced costs compared to the state-of-the-art models.

The speedup of the pseudo-rigid-body approach (using analytical traction expressions) relative to DNS simulations has been analyzed in our previous work (Appendix F of [30]), where a detailed discussion of the model's efficiency is provided. There, we showed that particle-resolved simulations (BEM) require on the order of 10^2 s per particle per time step, rendering such an approach infeasible for large particle numbers.[1] By contrast, our point-particle method requires only about 0.0003 s per particle per time step, making simulations with millions of particles computationally feasible. Note that the primary computational expense of the novel pseudo-rigid body approach lies in solving Newton iterations and evaluating the elliptic integrals involved in Roscoe's analytical traction expressions [24], which will be discussed in detail later.

1.2. Research gaps

To extend the novel pseudo-rigid body point-particle approach to particles of a more general stress-free shape, an obstacle arises due to the lack of analytical solutions, such as those studied by Roscoe [24], for non-ellipsoidal particles in flows. Existing models rely on parameters derived from expressions involving elliptical integrals, which are only available for a limited number of shapes, such as ellipsoidal particles. These expressions are both cumbersome to implement and computationally intensive to evaluate, depending on the employed framework.

As a result, having a Direct Numerical Simulation (DNS) database to efficiently determine the tractions exerted on the surface of arbitrarily shaped particles has a high potential, particularly for particles where no analytical expressions are available, i.e., non-ellipsoidal particles. However, since the tractions depend on both the particle shape and the local flow field, which is characterized by a velocity gradient matrix with nine coefficients, constructing a DNS database that covers all possible configurations is impractical due to the vast range of parameter variations (specifically for the velocity gradient tensor). If possible, a practical alternative is to identify form coefficients that are independent of the flow field. This would allow the database to be generated without sampling specific velocity gradient magnitudes, significantly reducing the parameter space (to only the particle shape parameters) while ensuring applicability to arbitrary global flow conditions.

[1] These computations were carried out on a laptop running Windows 11 Pro (64-bit), equipped with an AMD Ryzen 7 5800H CPU (3.2 GHz, 8 cores/16 threads), 64 GB RAM, and an NVIDIA GeForce RTX 3060 Laptop GPU with 6 GB VRAM.

1.3. Novelties

In this paper, we demonstrate the existence of form coefficients to determine the surface traction, which are independent of the magnitude of the velocity gradient, significantly reducing the number of parameters that need to be considered. This reduction enables the construction of a DNS database and, in turn, the generation of a data-driven surrogate approach. Specifically, we create a DNS database to train a neural network (NN) to capture the deformation of a soft ellipsoidal body in viscous flow. While the approach is initially developed for ellipsoidal particles, where analytical training data can be obtained and employed as a reference, it serves as a foundational step toward ultimately capturing soft non-spherical particles, for which analytical traction expressions, exerted from the flow on a soft particle, are unavailable.

2. Shape dynamics of a pseudo-rigid body

As a first step, we recall the shape dynamics of a pseudo-rigid body suspended in flows as presented in [30,31]. A brief overview of the pseudo-rigid body dynamics as proposed by Cohen and Muncaster [32] is provided in Appendix A including barycentric dynamics and the employed constitutive model.

To start with, consider a solid continuum body composed of physical points P, denoted by $\mathcal{B} = \{P\}$. Let $\bar{\mathcal{B}}_0$ represent the reference configuration (taken here as a unit sphere), $\mathcal{B}_0$ the material or stress-free configuration, and $\mathcal{B}_t$ the spatial or deformed configuration. Additionally, let $\bar{\rho}_0^{\mathrm{s}}$, ρ_0^{s} and ρ_t^{s} label the mass density (of the solid material) per unit volume in the reference configuration $\bar{\mathcal{B}}_0$, in the material configuration $\mathcal{B}_0$, and the spatial configuration $\mathcal{B}_t$, respectively. Furthermore, let $\bar{\boldsymbol{\Xi}}$, $\boldsymbol{\Xi}$ and $\boldsymbol{\xi}$ denote the relative reference, material and spatial positions, respectively.

To simplify the notation in the following, we use superscripts and subscripts $(\bullet)^{\mathrm{s}}$, $(\bullet)_{\mathrm{s}}$ and $(\bullet)^{\mathrm{f}}, (\bullet)_{\mathrm{f}}$ to indicate whether a property (superscript) or kinematic quantity (subscript) $(\bullet)$ pertains to the solid or the surrounding fluid, respectively, only when necessary to avoid ambiguity.

The shape dynamics equation of a pseudo-rigid body immersed in flow reads as

$$\dot{\boldsymbol{A}} \cdot \boldsymbol{\Theta} + \boldsymbol{P}\,\mathrm{vol}(\mathcal{B}_0) = \boldsymbol{M} \quad \text{with} \quad \boldsymbol{M} := \int_{\partial\mathcal{B}_0} \tilde{\boldsymbol{t}}_0 \otimes \boldsymbol{\Xi}\,\mathrm{d}A \quad \text{and} \quad \boldsymbol{A} = \dot{\boldsymbol{F}}. \tag{1}$$

In Eq. (1), $\boldsymbol{P}$ denotes the Piola stress, $\boldsymbol{M}$ labels the force dyad, $\tilde{\boldsymbol{t}}_0$ the traction (fluctuations), $\boldsymbol{F}$ the deformation gradient and $\boldsymbol{A}$ it's velocity. Note that $\boldsymbol{M}$ is in general a resultant of the dyadic moment of the bulk and surface force densities with $\boldsymbol{\Xi}$. However, in this work, we assume body forces are constant over $\mathcal{B}_0$, and consequently $\boldsymbol{M}$ depends solely on the traction (fluctuations) exerted by the flow on the particle surface. The Euler tensor $\boldsymbol{\Theta}$ of the pseudo-rigid body expands as

$$\boldsymbol{\Theta} := \int_{\mathcal{B}_0} \rho_0^{\mathrm{s}}\, \boldsymbol{\Xi} \otimes \boldsymbol{\Xi}\,\mathrm{d}V. \tag{2}$$

Note that the resultant force dyad $\boldsymbol{M}$ using the traction (fluctuations) acting on the undeformed body ($\partial\mathcal{B}_0$) relates to the force dyad $\boldsymbol{m}$ as

$$\boldsymbol{M} = \boldsymbol{m} \cdot \boldsymbol{F}^{-t} \quad \text{with} \quad \boldsymbol{m} = \int_{\partial\mathcal{B}_t} \tilde{\boldsymbol{t}}_t \otimes \boldsymbol{\xi}\,\mathrm{d}a. \tag{3}$$

Taken together, we observe that to describe the shape dynamics of a pseudo-rigid body, we need to determine the force dyad, which in turn depends on the traction (fluctuations). However, an analytical traction (fluctuations) expression is only available for a limited number of shapes. For ellipsoidal bodies immersed in (locally) Stokes flow, for example, one can employ the prominent (Jeffery [7] and) Roscoe [24] approach to determine $\tilde{\boldsymbol{t}}_t$. A detailed representation of this result is provided in our previous work [30,31]. However, evaluating this analytical expression is cumbersome as it involves various elliptic integrals, which are inconvenient to implement and constitute significant computational effort.

An alternative approach involves employing dedicated DNS simulations in combination with neural networks. This novel data-driven surrogate model allows to capture a large number of soft particles in viscous flow. The model bases on an affine deformations assumption (as inherent to pseudo-rigid bodies [32]), see [30,31] and is combined with Lagrangian point-particle tracking. The data-driven surrogate approach provides a foundational step to extend our novel soft particle tracking approach as presented in [30,31] beyond initially ellipsoidal shapes as for non-ellipsoidal particles analytical expressions for the tractions exerted by the flow do not exist. For convenience, we will next recall the analytical expressions available for tractions exerted on a soft (and rigid) initially ellipsoidal body immersed in (locally) Stokes flow, i.e., the Jeffery and Roscoe traction expressions.

2.1. Jeffery traction

By analytically solving Stokes flow equations for an incompressible Newtonian fluid (characterized by constant density ρ^{f} (note that due to incompressibility we need not distinguish between ρ_t^{f} and ρ_0^{f}), kinematic viscosity ν^{f}, and dynamic viscosity $\mu^{\mathrm{f}} = \rho^{\mathrm{f}}\nu^{\mathrm{f}}$) in the vicinity of an immersed ellipsoidal rigid body (particle), Jeffery [7] deduced the traction (fluctuation) $\tilde{\boldsymbol{t}}_t^{\mathrm{J}}$ exerted by the flow on the surface of the ellipsoidal rigid body in the format of

$$\tilde{\boldsymbol{t}}_t^{\mathrm{J}} = [-\tilde{p}(\boldsymbol{d}_{\mathrm{f}})\,\boldsymbol{i} + \mu^{\mathrm{f}}\,\tilde{\boldsymbol{s}}(\boldsymbol{d}_{\mathrm{f}}, \boldsymbol{w})] \cdot \boldsymbol{n}\,. \tag{4}$$

Here $\tilde{p}$ and $\tilde{\boldsymbol{s}}$ are a spatially constant coefficient and a spatially constant (non-symmetric) and deviatoric second-order tensor, respectively, $\boldsymbol{n}$ denotes the outwards pointing normal to the surface of the ellipsoid and $\boldsymbol{i}$ denotes the unit tensor. Note the dependencies of coefficient $\tilde{p} = \tilde{p}(\boldsymbol{d}_\mathrm{f})$ as well as the coefficients of $\tilde{\boldsymbol{s}} = \tilde{\boldsymbol{s}}(\boldsymbol{d}_\mathrm{f}, \boldsymbol{w})$ on the fluid rate of deformation tensor $\boldsymbol{d}_\mathrm{f}$ and the relative spin (vorticity) tensor $\boldsymbol{w} := \boldsymbol{w}_\mathrm{f} - \boldsymbol{w}_\mathrm{s}$ (with $\boldsymbol{w}_\mathrm{s}$ the spin tensor of the solid angular velocity vector). Eq. (4) is evaluated in the particle frame of reference (pFoR) that is oriented along the ellipsoidal half axes. Since the above Jeffery traction (fluctuation) is linear in the outwards pointing normal $\boldsymbol{n}$ to the surface of the ellipsoid, i.e. $\tilde{\boldsymbol{t}}_t = \tilde{\boldsymbol{\sigma}} \cdot \boldsymbol{n}$, it can finally be expressed in terms of a spatially uniform (constant) stress (further denoted as the Jeffery stress) $\tilde{\boldsymbol{\sigma}}^\mathrm{J}$ expanding as

$$\tilde{\boldsymbol{\sigma}}^\mathrm{J}(\boldsymbol{d}_\mathrm{f}, \boldsymbol{w}) = -\tilde{p}(\boldsymbol{d}_\mathrm{f})\, \boldsymbol{i} + \mu^\mathrm{f}\, \tilde{\boldsymbol{s}}(\boldsymbol{d}_\mathrm{f}, \boldsymbol{w})\,. \tag{5}$$

Observe that $\tilde{\boldsymbol{\sigma}}^\mathrm{J}$ depends on the fluid rate of deformation tensor $\boldsymbol{d}_\mathrm{f}$ as well as the relative spin tensor $\boldsymbol{w} := \boldsymbol{w}_\mathrm{f} - \boldsymbol{w}_\mathrm{s}$.

2.2. Jeffery-Roscoe traction

Roscoe [24] extended the analytical result of Jeffery [7] regarding the traction (fluctuation) $\tilde{\boldsymbol{t}}_t$ exerted by Stokes flow on the surface of an ellipsoidal rigid body to the case of an ellipsoidal deformable body. The final result reads

$$\tilde{\boldsymbol{t}}_t = \big[-\tilde{p}(\boldsymbol{d})\, \boldsymbol{i} + \mu^\mathrm{f} \left[\tilde{\boldsymbol{s}}(\boldsymbol{d}, \boldsymbol{w}) + 2\, \boldsymbol{d}_\mathrm{s}\right]\big] \cdot \boldsymbol{n}\,. \tag{6}$$

Observe that the Roscoe tractions are obtained using the coefficients $\tilde{p}(\boldsymbol{d})$ and $\tilde{\boldsymbol{s}}(\boldsymbol{d}, \boldsymbol{w})$, which now depend on the **relative** rate of deformation tensor $\boldsymbol{d} := \boldsymbol{d}_\mathrm{f} - \boldsymbol{d}_\mathrm{s}$ (recall also the previously already used definition of the relative spin (vorticity) tensor $\boldsymbol{w} := \boldsymbol{w}_\mathrm{f} - \boldsymbol{w}_\mathrm{s}$).

Here and below $\boldsymbol{d}_\mathrm{s}$ and $\boldsymbol{w}_\mathrm{s}$ denote the rate of deformation tensor and the spin tensor for the deformable ellipsoid, i.e. $\boldsymbol{d}_\mathrm{s} := \boldsymbol{l}_\mathrm{s}^\mathrm{sym}$ and $\boldsymbol{w}_\mathrm{s} := \boldsymbol{l}_\mathrm{s}^\mathrm{skw}$ with $\boldsymbol{l}_\mathrm{s}$ the spatial velocity gradient of the solid. For a deformable ellipsoid in Stokes flow, the rate of deformation tensor $\boldsymbol{d}_\mathrm{s}$ proves spatially homogeneous as confirmed by, e.g., Gao et al. [26,27], a kinematic condition compliant with the above assumptions of a pseudo-rigid body. Since the above Roscoe traction (fluctuation) is linear in the outwards pointing normal $\boldsymbol{n}$ to the surface of the ellipsoid, i.e. $\tilde{\boldsymbol{t}}_t = \tilde{\boldsymbol{\sigma}} \cdot \boldsymbol{n}$, it can finally be expressed in terms of a spatially uniform (constant) stress $\tilde{\boldsymbol{\sigma}}$ expanding as

$$\tilde{\boldsymbol{\sigma}}(\boldsymbol{d}, \boldsymbol{d}_\mathrm{s}, \boldsymbol{w}) = -\tilde{p}(\boldsymbol{d})\, \boldsymbol{i} + \mu^\mathrm{f} \left[\tilde{\boldsymbol{s}}(\boldsymbol{d}, \boldsymbol{w}) + 2\, \boldsymbol{d}_\mathrm{s}\right] = \tilde{\boldsymbol{\sigma}}^\mathrm{J}(\boldsymbol{d}, \boldsymbol{w}) + 2\mu^\mathrm{f}\, \boldsymbol{d}_\mathrm{s}\,. \tag{7}$$

Observe that the term $\tilde{\boldsymbol{\sigma}}^\mathrm{J}(\boldsymbol{d}, \boldsymbol{w}) = -\tilde{p}(\boldsymbol{d})\, \boldsymbol{i} + \mu^\mathrm{f} \tilde{\boldsymbol{s}}(\boldsymbol{d}, \boldsymbol{w})$ is given by Jeffery [7] when evaluated in terms of the relative rate of deformation tensor $\boldsymbol{d} := \boldsymbol{d}_\mathrm{f} - \boldsymbol{d}_\mathrm{s}$ (and, as already used before in the Jefferey expressions, the relative spin (vorticity) tensor $\boldsymbol{w} := \boldsymbol{w}_\mathrm{f} - \boldsymbol{w}_\mathrm{s}$). To summarize, the Roscoe stress expands in a Jeffery-type stress (with **relative** input) and a correction term $2\mu^\mathrm{f}\, \boldsymbol{d}_\mathrm{s}$. The key steps in the expression of the Roscoe traction (fluctuation) $\tilde{\boldsymbol{t}}_t$, [24], exerted on a deformable ellipsoid in a viscous flow are summarized in our previous work see [30]. Finally, by using the Jeffery-Roscoe stress, see Eq. (7), we can express the force dyad $\boldsymbol{m}$ as

$$\boldsymbol{m} = \tilde{\boldsymbol{\sigma}}\, \mathrm{vol}(\mathcal{B}_t) = \tilde{\boldsymbol{\sigma}}^\mathrm{J}(\boldsymbol{d}, \boldsymbol{w})\, \mathrm{vol}(\mathcal{B}_t) + 2\mu^\mathrm{f}\, \boldsymbol{d}_\mathrm{s}\, \mathrm{vol}(\mathcal{B}_t)\,. \tag{8}$$

Again, we want to highlight that $\boldsymbol{m}$ is expressed as a function of the Jeffery stress $\tilde{\boldsymbol{\sigma}}^\mathrm{J}(\boldsymbol{d}, \boldsymbol{w})$ with **relative** input (using the relative spin rate $\boldsymbol{d}$ and vorticity rate $\boldsymbol{w}$ as input) as well as a correction term $2\mu^\mathrm{f}\, \boldsymbol{d}_\mathrm{s}$.

3. Shape and flow dependency of the Jeffery stress tensor for soft deformable particles

The following section presents the analytical form of the Jeffery-Roscoe stress $\tilde{\boldsymbol{\sigma}}$, which is used to determine the resultant force dyad, $\boldsymbol{m} = \tilde{\boldsymbol{\sigma}}\, \mathrm{vol}(\mathcal{B}_t)$ (see Eq. (8)), a quantity that plays a central role in characterizing the deformation of a pseudo-rigid body.

3.1. Standard (Jeffery and) Roscoe expressions

To understand the different contributions to $\tilde{\boldsymbol{\sigma}}$ (and consequently to $\boldsymbol{m}$), we start by detailing the standard (Jeffery and) Roscoe expressions [30]. The Jeffery stress expands as

$$\tilde{\boldsymbol{\sigma}}^\mathrm{J} = -\big[p + 4\,\mu^\mathrm{f} \left[\alpha_0\, A + \beta_0\, B + \gamma_0\, C\right]\big]\, \boldsymbol{i} - 4\mu^\mathrm{f}\, \delta_0 \begin{bmatrix} A & H & G^\circ \\ H^\circ & B & F \\ G & F^\circ & C \end{bmatrix}, \tag{9}$$

with the parameters A, B, C expanding as

$$A = \upsilon_0 \big[2\, \alpha_0^\bullet\, d'_{11} - \beta_0^\bullet\, d'_{22} - \gamma_0^\bullet\, d'_{33}\big],\ B = \upsilon_0 \big[-\alpha_0^\bullet\, d'_{11} + 2\, \beta_0^\bullet\, d'_{22} - \gamma_0^\bullet\, d'_{33}\big] \ \text{ and } \ C = \upsilon_0 \big[-\alpha_0^\bullet\, d'_{11} - \beta_0^\bullet\, d'_{22} + 2\, \gamma_0^\bullet\, d'_{33}\big]\,, \tag{10}$$

where we introduce the shape-dependent pre-factors $\delta_0 = 2/\left[a_1\, a_2\, a_3\right]$ and $\upsilon_0 = \left[\alpha_0^\bullet\, \beta_0^\bullet + \beta_0^\bullet\, \gamma_0^\bullet + \gamma_0^\bullet\, \alpha_0^\bullet\right]^{-1}/6$ for abbreviation purposes. Furthermore, the parameters F, G, H and F°, G°, H° expand as

$$F = \upsilon_1 \big[\beta_0\, d'_{32} - c^2\, \alpha_0^\circ\, w'_{32}\big]\,, \qquad F^\circ = \upsilon_1 \big[\gamma_0\, d'_{32} + b^2\, \alpha_0^\circ\, w'_{32}\big]\,, \tag{11}$$

$$G = \upsilon_2 \big[\gamma_0\, d'_{13} - a^2\, \beta_0^\circ\, w'_{13}\big]\,, \qquad G^\circ = \upsilon_2 \big[\alpha_0\, d'_{13} + c^2\, \beta_0^\circ\, w'_{13}\big]\,, \tag{12}$$

$$H = \upsilon_3 \big[\alpha_0\, d'_{21} - b^2\, \gamma_0^\circ\, w'_{21}\big]\,, \qquad H^\circ = \upsilon_3 \big[\beta_0\, d'_{21} + a^2\, \gamma_0^\circ\, w'_{21}\big], \tag{13}$$

with shape-dependent pre-factors $\upsilon_1^{-1} = 2\, \alpha_0^\circ\, [a_2^2\, \beta_0 + a_3^2\, \gamma_0]$, $\upsilon_2^{-1} = 2\, \beta_0^\circ\, [a_3^2\, \gamma_0 + a_1^2\, \alpha_0]$ and $\upsilon_3^{-1} = 2\, \gamma_0^\circ\, [a_1^2\, \alpha_0 + a_2^2\, \beta_0]$.

Let's recall the definition of the shape-dependent parameters $\alpha_0^\bullet$, $\beta_0^\bullet$, and $\gamma_0^\bullet$. For this, we start by defining α_0, β_0, and γ_0 as well as α_0°, β_0°, and γ_0° as given in [33] for ellipsoidal particles. For ellipsoids with half axes a_1, a_2 and a_3 with $a_1 \geq a_2 \geq a_3$ the parameters α_0, β_0, and γ_0 expand as [33]

$$\alpha_0 = \int_0^\infty \frac{1}{[a_1^2+\Lambda]\,\Delta}\mathrm{d}\Lambda, \quad \beta_0 = \int_0^\infty \frac{1}{[a_2^2+\Lambda]\,\Delta}\mathrm{d}\Lambda \quad \text{and} \quad \gamma_0 = \int_0^\infty \frac{1}{[a_3^2+\Lambda]\,\Delta}\mathrm{d}\Lambda, \tag{14}$$

with $\Delta^2 := [a_1^2+\Lambda]\,[a_2^2+\Lambda]\,[a_3^2+\Lambda]$. Furthermore, the parameters α_0°, β_0°, and γ_0° expand as

$$\alpha_0^\circ = \int_0^\infty \frac{1}{[a_2^2+\Lambda]\,[a_3^2+\Lambda]\,\Delta}\mathrm{d}\Lambda, \quad \beta_0^\circ = \int_0^\infty \frac{1}{[a_3^2+\Lambda]\,[a_1^2+\Lambda]\,\Delta}\mathrm{d}\Lambda \quad \text{and} \quad \gamma_0^\circ = \int_0^\infty \frac{1}{[a_1^2+\Lambda]\,[a_2^2+\Lambda]\,\Delta}\mathrm{d}\Lambda, \tag{15}$$

and the parameters $\alpha_0^\bullet$, $\beta_0^\bullet$, and $\gamma_0^\bullet$ read as

$$\alpha_0^\bullet = \int_0^\infty \frac{\Lambda}{[a_2^2+\Lambda]\,[a_3^2+\Lambda]\,\Delta}\mathrm{d}\Lambda, \quad \beta_0^\bullet = \int_0^\infty \frac{\Lambda}{[a_3^2+\Lambda]\,[a_1^2+\Lambda]\,\Delta}\mathrm{d}\Lambda \quad \text{and} \quad \gamma_0^\bullet = \int_0^\infty \frac{\Lambda}{[a_1^2+\Lambda]\,[a_2^2+\Lambda]\,\Delta}\mathrm{d}\Lambda\,. \tag{16}$$

As shown in our previous work (see [31]) for prolate ellipsoids ($a_1 > a_2 = a_3$) and spheres ($a_1 = a_2 = a_3$) the shape-dependent parameters degenerate to simple expressions. However, in the case of triaxial ellipsoidal particles ($a_1 \neq a_2 \neq a_3$), the derived expressions still contain elliptical integrals, which are cumbersome to implement and evaluate depending on the employed framework.

3.2. Rearranged (Jeffery and) Roscoe expressions

In this section, we show that the standard Jeffery-Roscoe stress expression introduced in Section 3.1 can be reformulated as a superposition of distinct flow field contributions. For each flow field, the corresponding stress can be expressed as a product of a shape-dependent form coefficient $\hat{f}$ and the respective flow field term, with $\hat{f}$ obtained either from dedicated DNS simulations or, where available, from analytical expressions. This decomposition enables the training of the shape-dependent form coefficients using a neural network independently of the flow field. Note that without such a separation, the shape factors would depend on the full velocity-gradient tensor, whose nine components can vary significantly in magnitude across different applications. Including the velocity gradient as input to the neural network is therefore undesirable, as it would lead to an impractically large dataset. Thus, demonstrating that the stress can be decomposed in form and flow contributions is crucial, as it reduces the required dataset for the neural network to one that depends only on the form, i.e., the particle shape, and is independent of the local flow field.

3.2.1. Superposition of flow fields

Recall that the shape-dependent parameters $\alpha_0^\bullet$, $\beta_0^\bullet$, and $\gamma_0^\bullet$, as well as α_0, β_0, and γ_0, and α_0°, β_0°, and γ_0° (see Eqs. (14)–(16)) only depend on the particle shape, i.e., the particle half axis a_i, $i = 1, 2, 3$, and are independent of the local flow conditions. Thus, we can present the parameters A, B, C (see Eq. (10)) in an alternative form as

$$\begin{aligned} A = &\quad +2c_1 d'_{11} - c_2 d'_{22} - c_3 d'_{33} &&= A^d,\\ B = &\quad -c_1 d'_{11} + 2c_2 d'_{22} - c_3 d'_{33} &&= B^d,\\ C = &\quad -c_1 d'_{11} - c_2 d'_{22} + 2c_3 d'_{33} &&= C^d, \end{aligned} \tag{17}$$

with

$$c_1 = v_0 \alpha_0^\bullet, \qquad c_2 = v_0 \beta_0^\bullet \quad \text{and} \quad c_3 = v_0 \gamma_0^\bullet\,. \tag{18}$$

Taken together, we find that the parameters A, B, C depend on the particle shape (via the parameter c_i, $i = 1, 2, 3$) and the diagonal components of the deformation rate tensor coefficient $d_{(ii)}$ with $i = 1, 2, 3$ (no summation on i). To indicate the dependency on the deformation rate, we will employ the notation $A = A^d$ (and similarly for B and C) in the following. Next, we can expand F, G, H and F°, G°, H° (see Eqs. (11)–(13)) as

$$\begin{aligned} F &= v_1\beta_0\, d'_{32} - v_1 a_3^2\, \alpha_0^\circ\, w'_{32} &&= F^d + F^w,\\ F^\circ &= v_1\gamma_0\, d'_{32} + v_1 a_3^2\, \alpha_0^\circ\, w'_{32} &&= F^{\circ d} + F^{\circ w},\\ G &= v_2\gamma_0\, d'_{13} - v_2 a_1^2\, \beta_0^\circ\, w'_{13} &&= G^d + G^w,\\ G^\circ &= v_2\alpha_0\, d'_{13} + v_2 a_3^2\, \beta_0^\circ\, w'_{13} &&= G^{\circ d} + G^{\circ w},\\ H &= v_3\alpha_0\, d'_{21} - v_3 a_2^2\, \gamma_0^\circ\, w'_{21} &&= H^d + H^w,\\ H^\circ &= v_3\beta_0\, d'_{21} + v_3 a_1^2\, \gamma_0^\circ\, w'_{21} &&= H^{\circ d} + H^{\circ w}. \end{aligned} \tag{19}$$

Observe that for example F depends on contributions from both the (off-diagonal) rate of the deformation tensor coefficients (d_{32}) and the spin tensor coefficients (w_{32}) which are scaled by a shape-dependent factor $v_1\beta_0$ and $-v_1 a_3^2 \alpha_0^\circ$, respectively. Observe that similar relations hold for G, H, F°, G°, H°.

Taken together, we can eventually decompose $\tilde{\boldsymbol{\sigma}}^{\mathrm{J}}$ as

$$\tilde{\boldsymbol{\sigma}}^{\mathrm{J}} = \tilde{\boldsymbol{\sigma}}^{e} + \tilde{\boldsymbol{\sigma}}^{d} + \tilde{\boldsymbol{\sigma}}^{w}, \tag{20}$$

with

$$\underline{\tilde{\sigma}}^{e} = -\left[p + 4\,\mu^{\mathrm{f}}\left[\alpha_0\,A^{d} + \beta_0\,B^{d} + \gamma_0\,C^{d}\right]\right]\underline{i} - 4\mu^{\mathrm{f}}\delta_0\begin{bmatrix} A^{d} & 0 & 0 \\ 0 & B^{d} & 0 \\ 0 & 0 & C^{d} \end{bmatrix} \tag{21}$$

which accounts for the diagonal tensor coefficients, while the off-diagonal tensor components arising from both shear and spin contributions are accounted by

$$\underline{\tilde{\sigma}}^{d} = -4\mu^{\mathrm{f}}\delta_0\begin{bmatrix} 0 & H^{d} & G^{\circ d} \\ H^{\circ d} & 0 & F^{d} \\ G^{d} & F^{\circ d} & 0 \end{bmatrix} \quad \text{and} \quad \underline{\tilde{\sigma}}^{w} = -4\mu^{\mathrm{f}}\delta_0\begin{bmatrix} 0 & H^{w} & G^{\circ w} \\ H^{\circ w} & 0 & F^{w} \\ G^{w} & F^{\circ w} & 0 \end{bmatrix}. \tag{22}$$

In summary, $\tilde{\boldsymbol{\sigma}}^{\mathrm{J}}$ expands as a superposition of contributions from expansional flow (superscript e), deformation rate (superscript d), and spin rate (superscript w).

3.2.2. Spin tensor contributions

Next, we first analyze the spin tensor stress contribution $\tilde{\boldsymbol{\sigma}}^{w}$. By employing the expressions presented in Eq. (19), $\tilde{\boldsymbol{\sigma}}^{w}$ reads as

$$\underline{\tilde{\sigma}}^{w} = -4\mu^{\mathrm{f}}\delta_0\begin{bmatrix} 0 & H^{w} & G^{\circ w} \\ H^{\circ w} & 0 & F^{w} \\ G^{w} & F^{\circ w} & 0 \end{bmatrix} = \mu^{\mathrm{f}}\begin{bmatrix} 0 & \hat{f}_1^{w} w'_{12} & \hat{f}_4^{w} w'_{13} \\ \hat{f}_2^{w} w'_{21} & 0 & \hat{f}_5^{w} w'_{23} \\ \hat{f}_3^{w} w'_{31} & \hat{f}_6^{w} w'_{32} & 0 \end{bmatrix}. \tag{23}$$

This can be further decomposed as

$$\underline{\tilde{\sigma}}^{w} = \mu^{\mathrm{f}}\begin{bmatrix} 0 & \hat{f}_1^{w} w'_{12} & 0 \\ \hat{f}_2^{w} w'_{21} & 0 & 0 \\ 0 & 0 & 0 \end{bmatrix} + \mu^{\mathrm{f}}\begin{bmatrix} 0 & 0 & \hat{f}_4^{w} w'_{13} \\ 0 & 0 & 0 \\ \hat{f}_3^{w} w'_{31} & 0 & 0 \end{bmatrix} + \mu^{\mathrm{f}}\begin{bmatrix} 0 & 0 & 0 \\ 0 & 0 & \hat{f}_5^{w} w'_{23} \\ 0 & \hat{f}_6^{w} w'_{32} & 0 \end{bmatrix}, \tag{24}$$

i.e., into a superposition of three main rotation contributions around the principal particle axes, where the parameters $\hat{f}_i^{w}$ with $i = 1, 2, \ldots 6$ represent the corresponding non-dimensional form coefficients. These form coefficients expand as

$$\begin{aligned} \hat{f}_1^{w} &= -4\delta_0\left[-v_3 a_2^2 \gamma_0^{\circ}\right], & \hat{f}_2^{w} &= -4\delta_0\left[+v_3 a_1^2 \gamma_0^{\circ}\right], & \hat{f}_3^{w} &= -4\delta_0\left[-v_2 a_1^2 \beta_0^{\circ}\right], \\ \hat{f}_4^{w} &= -4\delta_0\left[+v_2 a_3^2 \beta_0^{\circ}\right], & \hat{f}_5^{w} &= -4\delta_0\left[-v_1 a_3^2 \alpha_0^{\circ}\right], & \hat{f}_6^{w} &= -4\delta_0\left[+v_1 a_2^2 \alpha_0^{\circ}\right]. \end{aligned} \tag{25}$$

Together, we need to determine six form coefficients to describe the contribution of rotational flow to the force dyad exerted on the particle and consequently to the shape dynamics. We observe that this can be achieved by choosing a specific flow field specified by a velocity gradient only possessing two non-zero rotational contributions. Consequently, we employ the following non-dimensional velocity gradients expanding in matrix form as

$$\underline{l}_f^{w_1} = \begin{bmatrix} 0 & 1 & 0 \\ -1 & 0 & 0 \\ 0 & 0 & 0 \end{bmatrix}, \quad \underline{l}_f^{w_2} = \begin{bmatrix} 0 & 0 & 1 \\ 0 & 0 & 0 \\ -1 & 0 & 0 \end{bmatrix}, \quad \underline{l}_f^{w_3} = \begin{bmatrix} 0 & 0 & 0 \\ 0 & 0 & 1 \\ 0 & -1 & 0 \end{bmatrix}. \tag{26}$$

The resulting form coefficients are displayed depending on the respective particle shape (aspect ratios for ellipsoidal particles λ_1, λ_2 with $\lambda_1 \geq \lambda_2$) in Fig. 1.

Note that results for $\lambda_2 > \lambda_1$ are not included, since in the particle frame of reference (pFoR), which is aligned with the particle's long axis, this case corresponds to the particle being associated with one of the other two flow configurations (i.e., instead of the first shear flow configuration, the case is then represented in the second or third configuration).

Across all three rotational-flow contributions, the computed form coefficients are strictly positive, but their magnitudes differ substantially depending on both the coefficient index and the particle aspect ratios. For $\underline{l}_f^{w_1}$, the coefficients $\hat{f}_1^{w}$ and $\hat{f}_2^{w}$ display markedly different scales: while $\hat{f}_1^{w}$ remains relatively small across the full range of (λ_1, λ_2), $\hat{f}_2^{w}$ increases sharply with particle elongation and can exceed values of 60 for strongly prolate ellipsoids (e.g., $\lambda_1 = 10$, $\lambda_2 = 1$). A similar disparity is observed for $\underline{l}_f^{w_2}$, where $\hat{f}_3^{w}$ is limited to values below 3, whereas $\hat{f}_4^{w}$ grows rapidly for elongated shapes, again reaching magnitudes above 60. Finally, for $\underline{l}_f^{w_3}$, the coefficients $\hat{f}_5^{w}$ and $\hat{f}_6^{w}$ exhibit a comparable difference, with $\hat{f}_6^{w}$ attaining values an order of magnitude larger than $\hat{f}_5^{w}$. These observations emphasize two important points: (i) the anisotropic response of the particle to rotational flow is strongly dependent on the aspect ratio, with certain coefficients becoming dominant for elongated geometries, and (ii) the relative weighting of the coefficients within the considered rotational flow configuration varies significantly, indicating that different flow modes excite distinct components of the stress response.

3.2.3. Shear tensor contributions

In a similar fashion to the spin tensor stress contribution, we may expand the deformation rate stress contribution $\tilde{\boldsymbol{\sigma}}^{d}$, which results as

$$\underline{\tilde{\sigma}}^{d} = -4\mu^{\mathrm{f}}\delta_0\begin{bmatrix} 0 & H^{w} & G^{\circ w} \\ H^{\circ w} & 0 & F^{w} \\ G^{w} & F^{\circ w} & 0 \end{bmatrix} = \mu^{\mathrm{f}}\begin{bmatrix} 0 & \hat{f}_1^{d} d'_{12} & 0 \\ \hat{f}_2^{d} d'_{21} & 0 & 0 \\ 0 & 0 & 0 \end{bmatrix} + \mu^{\mathrm{f}}\begin{bmatrix} 0 & 0 & \hat{f}_4^{d} d'_{13} \\ 0 & 0 & 0 \\ \hat{f}_3^{d} d'_{31} & 0 & 0 \end{bmatrix} + \mu^{\mathrm{f}}\begin{bmatrix} 0 & 0 & 0 \\ 0 & 0 & \hat{f}_5^{d} d'_{23} \\ 0 & \hat{f}_6^{d} d'_{32} & 0 \end{bmatrix}, \tag{27}$$

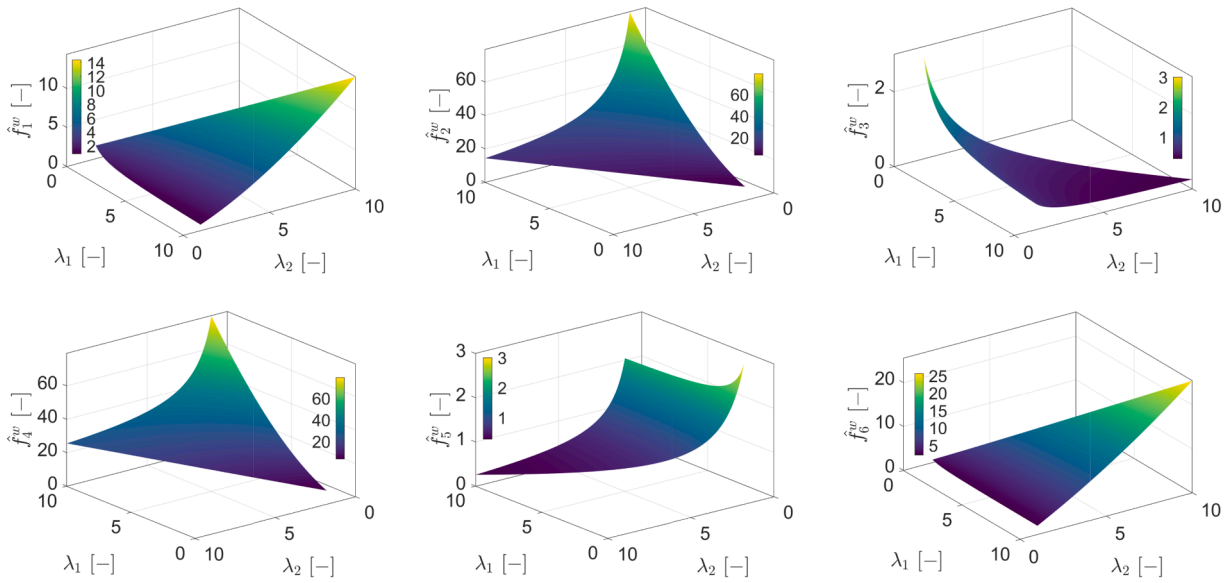

Fig. 1. Visualization of the form coefficients $\hat{f}_i^w$ with $i = 1, \dots 6$ resulting from rotational flow contributions ($\underline{l}_f^{w_1}, \underline{l}_f^{w_2}, \underline{l}_f^{w_3}$). The presented coefficients are obtained using analytical expressions. Note that for display purposes, the orientation of the axis is not chosen identically for all presented form coefficients.

i.e., a superposition of three main shear flow contributions around the principal particle axis, where $\hat{f}_i^d$ with $i = 1, 2, \dots 6$ represent the corresponding non-dimensional form coefficients. These form coefficients expand as

$$\begin{aligned} \hat{f}_1^d &= -4\delta_0[v_3\alpha_0], \quad \hat{f}_2^d = -4\delta_0[v_3\beta_0], \quad \hat{f}_3^d = -4\delta_0[v_2\gamma_0], \\ \hat{f}_4^d &= -4\delta_0[v_2\alpha_0], \quad \hat{f}_5^d = -4\delta_0[v_1\beta_0], \quad \hat{f}_6^d = -4\delta_0[v_1\gamma_0]. \end{aligned} \tag{28}$$

Taken together, we need to determine six form coefficients to describe shear flow contribution to the force dyad exerted on the particle and consequently to the shape dynamics. We observe that this can be achieved conveniently by choosing a specific flow field specified by a velocity gradient only possessing two non-zero shear contributions. Consequently, we employ the following three non-dimensional velocity gradients expanding in matrix form as

$$\underline{l}_f^{d_1} = \begin{bmatrix} 0 & 1 & 0 \\ 1 & 0 & 0 \\ 0 & 0 & 0 \end{bmatrix} \quad \underline{l}_f^{d_2} = \begin{bmatrix} 0 & 0 & 1 \\ 0 & 0 & 0 \\ 1 & 0 & 0 \end{bmatrix} \quad \underline{l}_f^{d_3} = \begin{bmatrix} 0 & 0 & 0 \\ 0 & 0 & 1 \\ 0 & 1 & 0 \end{bmatrix}. \tag{29}$$

The analytically obtained form coefficients are shown in Fig. 2 as functions of the particle aspect ratios λ_1 and λ_2. As before, only results with $\lambda_1 \geq \lambda_2$ are included, since cases with $\lambda_2 > \lambda_1$ correspond to particles that are accounted for in one of the other two shear-flow configurations.

In contrast to the coefficients obtained for the rotational-flow contributions (Fig. 1), the deformation-rate (shear-flow) coefficients reveal a somewhat different distribution of magnitudes across the six form coefficients. Specifically, the trend for $\hat{f}_3^d$ and $\hat{f}_3^w$ varies strongly. While all (shear-flow) coefficients remain positive, they exhibit pronounced disparities in scale. For instance, $\hat{f}_1^d$ and $\hat{f}_6^d$ grow moderately with increasing elongation (similar to the rotational-flow coefficients) and reach values on the order of 20–25, whereas $\hat{f}_2^d$ and $\hat{f}_4^d$ rise much more strongly, exceeding 80 for highly prolate shapes (e.g., $\lambda_1 = 10$, $\lambda_2 = 1$). By contrast, $\hat{f}_3^d$ and $\hat{f}_5^d$ remain comparatively small, saturating at values of about 4–5.

This strong deviation between shear-flow form coefficients is similar to what was observed in the rotational-flow case, but here the contrast is even more pronounced: the dominant coefficients ($\hat{f}_2^d$, $\hat{f}_4^d$) scale strongly with particle elongation, whereas the weaker coefficients remain nearly negligible in comparison. This highlights that shear-driven stresses are likewise to rotational-driven stresses highly sensitive to particle anisotropy, with certain stress components being strongly amplified while others remain comparatively minor.

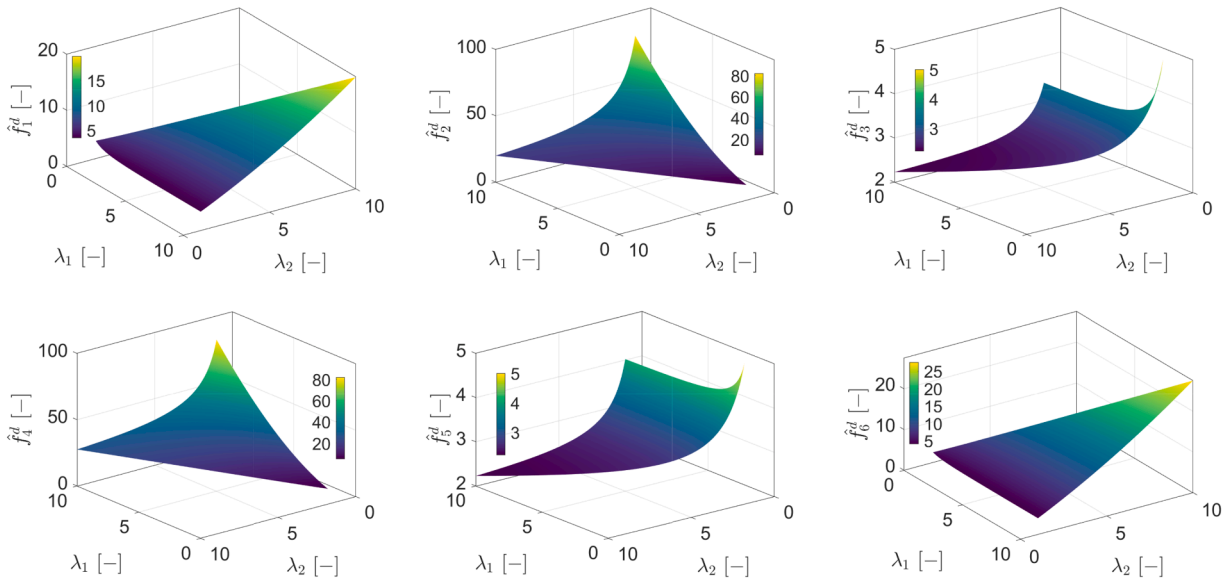

Fig. 2. Visualization of form coefficients $\hat{f}_i^d$ with $i = 1, \dots 6$ resulting from shear flow contributions ($\underline{l}_f^{d_1}$, $\underline{l}_f^{d_2}$, $\underline{l}_f^{d_3}$). The presented coefficients are obtained using analytical expressions. Note that for display purposes, the orientation of the axes is not chosen identically for all presented form coefficients.

3.2.4. Expansional flow contributions

Lastly, we need to analyze $\tilde{\boldsymbol{\sigma}}^e$ (see Eq. (21)), i.e., the expansional flow contribution to the Jeffery's stress $\tilde{\boldsymbol{\sigma}}^{\mathrm{J}}$. This term expands as

$$\begin{aligned}\underline{\tilde{\sigma}}^{\mathrm{e}} &= -\left[p + 4\,\mu^{\mathrm{f}}\left[\alpha_0\,A^d + \beta_0\,B^d + \gamma_0\,C^d\right]\right]\underline{i} - 4\mu^{\mathrm{f}}\delta_0\begin{bmatrix}A^d & 0 & 0\\ 0 & B^d & 0\\ 0 & 0 & C^d\end{bmatrix}\\ &= -p\underline{i} - 4\,\mu^{\mathrm{f}}\left[\alpha_0\,A^d + \beta_0\,B^d + \gamma_0\,C^d\right]\underline{i} - 4\mu^{\mathrm{f}}\delta_0\begin{bmatrix}A^d & 0 & 0\\ 0 & B^d & 0\\ 0 & 0 & C^d\end{bmatrix},\end{aligned} \tag{30}$$

which can be rewritten as

$$\begin{aligned}\underline{\tilde{\sigma}}^{\mathrm{e}} &= -p\underline{i}\\ &\quad - 4\mu^{\mathrm{f}}\begin{bmatrix}\left[\alpha_0+\delta_0\right]A^d + \beta_0\,B^d + \gamma_0\,C^d & 0 & 0\\ 0 & \alpha_0\,A^d + \left[\beta_0+\delta_0\right]B^d + \gamma_0\,C^d & 0\\ 0 & 0 & \alpha_0\,A^d + \beta_0\,B^d + \left[\gamma_0+\delta_0\right]C^d\end{bmatrix}\\ &= -p\underline{i} + \mu^{\mathrm{f}}\begin{bmatrix}\hat{f}_1^e d'_{11} + \hat{f}_2^e d'_{22} + \hat{f}_3^e d'_{33} & 0 & 0\\ 0 & \hat{f}_4^e d'_{11} + \hat{f}_5^e d'_{22} + \hat{f}_6^e d'_{33} & 0\\ 0 & 0 & \hat{f}_7^e d'_{11} + \hat{f}_8^e d'_{22} + \hat{f}_9^e d'_{33}\end{bmatrix}.\end{aligned} \tag{31}$$

Note that the coefficient $\delta_0 = 2/\left[a_1\,a_2\,a_3\right]$ possesses identical dimension as α_0, β_0 and γ_0, i.e. $\left[m^{-3}\right]$. Next, we consider the diagonal terms separately, inserting the expressions presented in Eq. (17), and regrouping, we obtain

$$\begin{aligned}&\left[\alpha_0+\delta_0\right]A^d + \beta_0\,B^d + \gamma_0\,C^d =\\ &\left[\alpha_0+\delta_0\right]\left[2c_1d'_{11} - c_2d'_{22} - c_3d'_{33}\right] + \beta_0\left[-c_1d'_{11} + 2c_2d'_{22} - c_3d'_{33}\right] + \gamma_0\left[-c_1d'_{11} - c_2d'_{22} + 2c_3d'_{33}\right] =\\ &d'_{11}\left[\left[\alpha_0+\delta_0\right]2 - \beta_0 - \gamma_0\right]c_1 + d'_{22}\left[-\left[\alpha_0+\delta_0\right] + 2\beta_0 - \gamma_0\right]c_2 + d'_{33}\left[-\left[\alpha_0+\delta_0\right] - \beta_0 + 2\gamma_0\right]c_3\\ &\hat{f}_1^e d'_{11} + \hat{f}_2^e d'_{22} + \hat{f}_3^e d'_{33}\end{aligned} \tag{32}$$

and

$$\begin{aligned}&\alpha_0\,A^d + \left[\beta_0+\delta_0\right]B^d + \gamma_0\,C^d =\\ &d'_{11}\left[2\alpha_0 - \left[\beta_0+\delta_0\right] - \gamma_0\right]c_1 + d'_{22}\left[-\alpha_0 + 2\left[\beta_0+\delta_0\right] - \gamma_0\right]c_2 + d'_{33}\left[-\alpha_0 - \left[\beta_0+\delta_0\right] + 2\gamma_0\right]c_3 =\\ &\hat{f}_4^e d'_{11} + \hat{f}_5^e d'_{22} + \hat{f}_6^e d'_{33}\end{aligned} \tag{33}$$

and

$$\begin{aligned}&\alpha_0\, A^d + \beta_0\, B^d + \left[\gamma_0 + \delta_0\right] C^d = \\ &d'_{11}\left[2\alpha_0 - \beta_0 - \left[\gamma_0 + \delta_0\right]\right]c_1 + d'_{22}\left[-\alpha_0 + 2\beta_0 - \left[\gamma_0 + \delta_0\right]\right]c_2 + d'_{33}\left[-\alpha_0 - \beta_0 + 2\left[\gamma_0 + \delta_0\right]\right]c_3 = \\ &\hat{f}^e_7 d'_{11} + \hat{f}^e_8 d'_{22} + \hat{f}^e_9 d'_{22}\,.\end{aligned} \tag{34}$$

Collectively, this leads to the following analytical expressions for the form coefficients

$$\begin{aligned}\hat{f}^e_1 &= \left[\left[\alpha_0 + \delta_0\right]2 - \beta_0 - \gamma_0\right]c_1\,,\\ \hat{f}^e_2 &= \left[-\left[\alpha_0 + \delta_0\right] + 2\beta_0 - \gamma_0\right]c_2\,,\\ \hat{f}^e_3 &= \left[-\left[\alpha_0 + \delta_0\right] - \beta_0 + 2\gamma_0\right]c_3\,,\\ \hat{f}^e_4 &= \left[2\alpha_0 - \left[\beta_0 + \delta_0\right] - \gamma_0\right]c_1\,,\\ \hat{f}^e_5 &= \left[-\alpha_0 + 2\left[\beta_0 + \delta_0\right] - \gamma_0\right]c_2\,,\\ \hat{f}^e_6 &= \left[-\alpha_0 - \left[\beta_0 + \delta_0\right] + 2\gamma_0\right]c_3\,,\\ \hat{f}^e_7 &= \left[2\alpha_0 - \beta_0 - \left[\gamma_0 + \delta_0\right]\right]c_1\,,\\ \hat{f}^e_8 &= \left[-\alpha_0 + 2\beta_0 - \left[\gamma_0 + \delta_0\right]\right]c_2\,,\\ \hat{f}^e_9 &= \left[-\alpha_0 - \beta_0 + 2\left[\gamma_0 + \delta_0\right]\right]c_3\,.\end{aligned} \tag{35}$$

Note that in the case of ellipsoidal particles, the parameters α_0, β_0, and γ_0 can be obtained according to Eq. (15), i.e., by solving elliptical integrals. Furthermore, analysis of the above equations reveals that $\hat{f}^e_2 = \hat{f}^e_8$, $\hat{f}^e_3 = \hat{f}^e_6$, $\hat{f}^e_4 = \hat{f}^e_7$.

This implies that, instead of nine form coefficients, only six need to be determined to characterize the contribution of extensional flow to the force dyad acting on the particle and, consequently, to its shape dynamics. Let's next consider three different sets of expansional flow fields, with the corresponding non-dimensional velocity gradient expanding in matrix form as

$$\underline{l}^{e_1}_f = \begin{bmatrix}1 & 0 & 0\\ 0 & -0.5 & 0\\ 0 & 0 & -0.5\end{bmatrix},\quad \underline{l}^{e_2}_f = \begin{bmatrix}-0.5 & 0 & 0\\ 0 & 1 & 0\\ 0 & 0 & -0.5\end{bmatrix},\quad \underline{l}^{e_3}_f = \begin{bmatrix}-0.5 & 0 & 0\\ 0 & -0.5 & 0\\ 0 & 0 & 1\end{bmatrix}. \tag{36}$$

Consequently, we arrive at

$$\begin{aligned}\hat{f}^e_1 - 0.5\hat{f}^e_2 - 0.5\hat{f}^e_3 &= \tilde{\sigma}^e_{11}(\underline{l}^{e_1}_f) = \varsigma_1\,,\\ \hat{f}^e_4 - 0.5\hat{f}^e_5 - 0.5\hat{f}^e_3 &= \tilde{\sigma}^e_{22}(\underline{l}^{e_1}_f) = \varsigma_2\,,\\ \hat{f}^e_4 - 0.5\hat{f}^e_2 - 0.5\hat{f}^e_9 &= \tilde{\sigma}^e_{33}(\underline{l}^{e_1}_f) = \varsigma_3\,,\\ -0.5\hat{f}^e_1 + \hat{f}^e_2 - 0.5\hat{f}^e_3 &= \tilde{\sigma}^e_{11}(\underline{l}^{e_2}_f) = \varsigma_4\,,\\ -0.5\hat{f}^e_4 + \hat{f}^e_5 - 0.5\hat{f}^e_3 &= \tilde{\sigma}^e_{22}(\underline{l}^{e_2}_f) = \varsigma_5\,,\\ -0.5\hat{f}^e_4 + \hat{f}^e_2 - 0.5\hat{f}^e_9 &= \tilde{\sigma}^e_{33}(\underline{l}^{e_2}_f) = \varsigma_6\,,\\ -0.5\hat{f}^e_1 - 0.5\hat{f}^e_2 + \hat{f}^e_3 &= \tilde{\sigma}^e_{11}(\underline{l}^{e_3}_f) = \varsigma_7\,,\\ -0.5\hat{f}^e_4 - 0.5\hat{f}^e_5 + \hat{f}^e_3 &= \tilde{\sigma}^e_{22}(\underline{l}^{e_3}_f) = \varsigma_8\,,\\ -0.5\hat{f}^e_4 - 0.5\hat{f}^e_2 + \hat{f}^e_9 &= \tilde{\sigma}^e_{33}(\underline{l}^{e_3}_f) = \varsigma_9\,.\end{aligned} \tag{37}$$

Analyzing the above equations reveals that $\varsigma_1 + \varsigma_4 + \varsigma_7 = 0$, $\varsigma_2 + \varsigma_5 + \varsigma_8 = 0$, and $\varsigma_3 + \varsigma_6 + \varsigma_9 = 0$. As a result, the final set of equations involving $\underline{l}^{e_3}_f$ ($\rightarrow \varsigma_7,\ \varsigma_8,\ \varsigma_9$) does not yield additional information, since these terms can be derived from the equations involving $\underline{l}^{e_1}_f$ and $\underline{l}^{e_2}_f$, i.e. $\varsigma_7 = -\varsigma_1 - \varsigma_4$. Therefore, the expressions based on $\underline{l}^{e_3}_f$ are not required to determine the form coefficients $\hat{f}^e_i$. This reduces the system of equations to

$$\begin{aligned}\hat{f}^e_1 - 0.5\hat{f}^e_2 - 0.5\hat{f}^e_3 &= \tilde{\sigma}_{11}(\underline{l}^{e_1}_f) = \varsigma_1\,,\\ \hat{f}^e_4 - 0.5\hat{f}^e_5 - 0.5\hat{f}^e_3 &= \tilde{\sigma}_{22}(\underline{l}^{e_1}_f) = \varsigma_2\,,\\ \hat{f}^e_4 - 0.5\hat{f}^e_2 - 0.5\hat{f}^e_9 &= \tilde{\sigma}_{33}(\underline{l}^{e_1}_f) = \varsigma_3\,,\\ -0.5\hat{f}^e_1 + \hat{f}^e_2 - 0.5\hat{f}^e_3 &= \tilde{\sigma}_{11}(\underline{l}^{e_2}_f) = \varsigma_4\,,\\ -0.5\hat{f}^e_4 + \hat{f}^e_5 - 0.5\hat{f}^e_3 &= \tilde{\sigma}_{22}(\underline{l}^{e_2}_f) = \varsigma_5\,,\\ -0.5\hat{f}^e_4 + \hat{f}^e_2 - 0.5\hat{f}^e_9 &= \tilde{\sigma}_{33}(\underline{l}^{e_2}_f) = \varsigma_6\,.\end{aligned} \tag{38}$$

We can now construct a linear system of the form $\underline{A}\,\underline{x} = \underline{\varsigma}$, where $\underline{x}$ contains the unknown form coefficients $\hat{f}^e_i$ ($i = 1, 2, 3, 4, 5, 9$). Upon doing so, it becomes evident that matrix $\underline{A}$ is not invertible, as the sum of each row is zero, which indicates a linear dependence among the equations. Specifically, the matrix $\underline{A}$ has rank 5. As a result, without any further relation, it is not possible to directly extract the analytical form coefficients $\hat{f}^e_i$ from the DNS simulations. However, we find that due to the incompressibility condition ($l'_{11} + l'_{22} + l'_{33} = 0$) imposed in the Jeffery solution, the exact values of $\hat{f}^e_i$ are not required. Instead, a shifted set of values $\hat{f}^e_i + \Delta\hat{f}^e$ suffices for modeling the tractions on the particle surface, since a constant offset $\Delta\hat{f}^e$ does not affect the final traction outcome as demonstrated in the following

$$\underbrace{\left[\hat{f}^e_1 + \Delta\hat{f}^e\right]}_{\hat{f}^{e*}_1} l'_{11} + \underbrace{\left[\hat{f}^e_2 + \Delta\hat{f}^e\right]}_{\hat{f}^{e*}_2} l'_{22} + \underbrace{\left[\hat{f}^e_3 + \Delta\hat{f}^e\right]}_{\hat{f}^{e*}_3} l'_{33} = \left[\hat{f}^e_1 l'_{11} + \hat{f}^e_2 l'_{22} + \hat{f}^e_3 l'_{33}\right] + \Delta\hat{f}^e \underbrace{\left[l'_{11} + l'_{22} + l'_{33}\right]}_{0} = \varsigma\,. \tag{39}$$

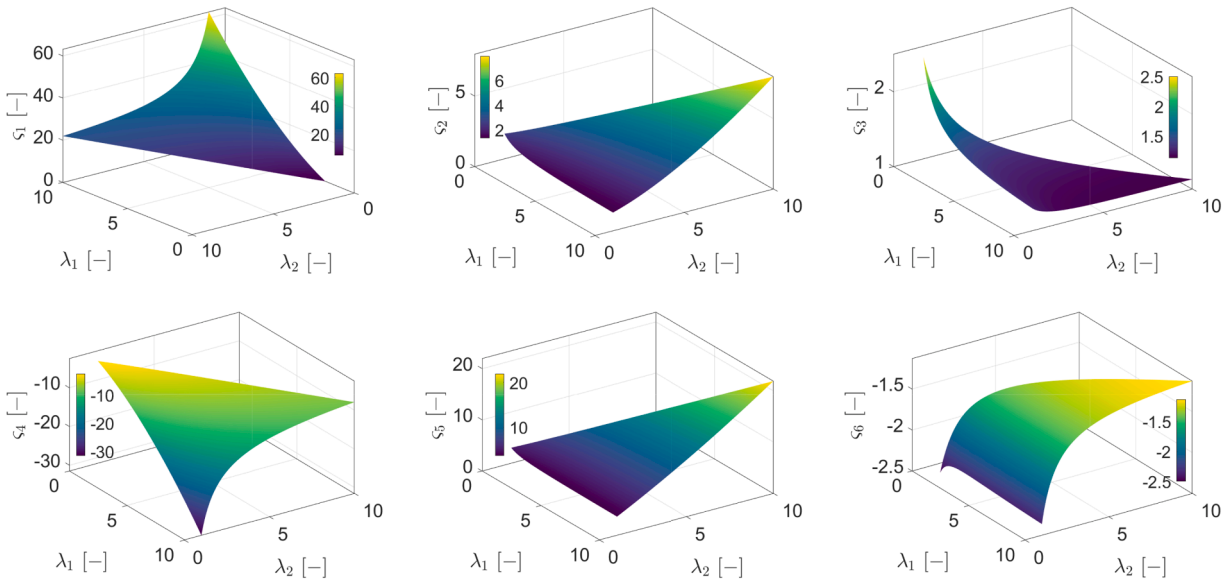

Fig. 3. Analytical force dyad coefficients $\varsigma_1 - \varsigma_6$ resulting from the two expansional flow configurations chosen ($\underline{l}_f^{e_1}, \underline{l}_f^{e_2}$). The presented coefficients are obtained using analytical expressions. Note that for display purposes, the orientation of the axes is not chosen identically for all presented form coefficients.

Therefore, the stress (or traction) matrix remains invariant under a shift by a constant $\Delta\hat{f}^e$, meaning the stress state is unaffected. This allows us to choose $\Delta\hat{f}^e$ arbitrarily and conveniently. In the following, we employ $\Delta\hat{f}^e = -\hat{f}^e_9$, as then $\hat{f}^{e*}_9 = 0$. With this choice, we are able to solve for the (adjusted) form coefficients $\hat{f}^{e*}_i$ ($i = 1, \dots 5$). The resulting expressions for these are given below

$$
\begin{aligned}
\hat{f}^{e*}_1 &= 2\varsigma_1 - [8\varsigma_2]/3 + 2\varsigma_3 + 2\varsigma_4 - [4\varsigma_5]/3, \\
\hat{f}^{e*}_2 &= [4\varsigma_1]/3 - [8\varsigma_2]/3 + 2\varsigma_3 + [8\varsigma_4]/3 - [4\varsigma_5]/3, \\
\hat{f}^{e*}_3 &= [2\varsigma_1]/3 - [8\varsigma_2]/3 + 2\varsigma_3 + [4\varsigma_4]/3 - [4\varsigma_5]/3, \\
\hat{f}^{e*}_4 &= [2\varsigma_1]/3 - [4\varsigma_2]/3 + 2\varsigma_3 + [4\varsigma_4]/3 - [2\varsigma_5]/3, \\
\hat{f}^{e*}_5 &= [2\varsigma_1]/3 - 2\varsigma_2 + 2\varsigma_3 + [4\varsigma_4]/3 .
\end{aligned}
\tag{40}
$$

In the following, we first present the traction results ς_i obtained from Jeffery's analytical expression [7], as illustrated in Fig. 3. This approach is limited to ellipsoidal shapes, as analytical traction expressions are not available for more complex particle geometries. As shown in Fig. 3, the form coefficients associated with expansional flow also exhibit considerable variation depending on particle shape. Moreover, when comparing the magnitudes of these parameters, we observe significant differences among them. For instance, the value of ς_1 can reach values up to 60, while for example ς_2 and ς_3 stay below 10.

By inserting the coefficients ς_i (obtained from Eq. (38)) in Eq. (40), we obtain the expansional flow form coefficients $\hat{f}^{e*}_i$, which are displayed in Fig. 4.

In contrast to the rotational- and shear-flow cases, where all coefficients were strictly positive, the expansional coefficients exhibit both positive and negative values depending on the particle shape. The magnitudes of the expansional coefficients are generally more moderate compared to the shear-driven coefficients, but still display significant differences across components. For instance, $\hat{f}^{e*}_1$ attains values exceeding 40 for elongated particles, whereas $\hat{f}^{e*}_2$ and $\hat{f}^{e*}_3$ can reach values as low as -40 for the same shapes, showing that negative stress contributions can occur depending on the component considered. By comparison, $\hat{f}^{e*}_4$ and $\hat{f}^{e*}_5$ remain smaller in magnitude, typically between 20 and 0.

Taken together, these results highlight a distinct difference compared to the rotational and shear cases: while those stresses showed a systematic imbalance in magnitude across coefficients (with dominant and nearly negligible terms), the expansional coefficients are characterized instead by strong sign asymmetry, with some components becoming strongly positive while others are equally strongly negative. This emphasizes that expansional flow excites a qualitatively different response, where particle anisotropy not only amplifies certain coefficients but can also change the sign of the contribution to the overall stress.

3.3. Direct numerical simulations

In the case of generic particles, analytical expressions for the form coefficients are not present. Consequently, we have to employ DNS to obtain the tractions exerted on the particle. These DNS results can consequently be employed to obtain the form coefficients for shear flow, rotational flow as well as expansional flow. Recall that for shear flow and rotational flow, we can obtain these coefficients straightforwardly, while for expansional flow, we require Eq. (40).

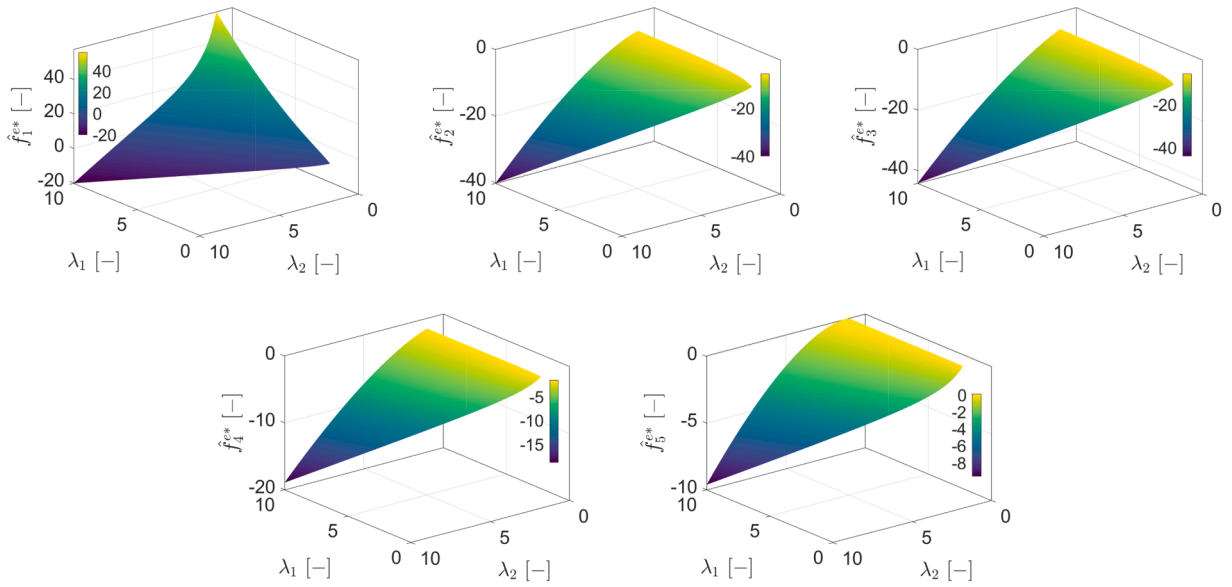

Fig. 4. Visualization of the form coefficients $\hat{f}_i^{e*}$ with $i = 1, \dots 5$ resulting from expansional flow contributions. The presented coefficients are obtained using analytical expressions.

3.3.1. Governing equations

Let us consider soft micro-particles that possess a particle size smaller than the Kolmogorov length scale of the flow. Typically, this also results in a correspondingly small particle Stokes number (Stk), indicating that the particle trajectory closely follows the flow. The Stokes number is obtained using

$$\mathrm{Stk} = \frac{1}{18}\frac{\rho^{\mathrm{s}}}{\rho^{\mathrm{f}}}\left[\mathrm{d_{eq}}/\eta_{\mathrm{K}}\right]^2, \tag{41}$$

where ρ^{s} and ρ^{f} are the particle and fluid densities respectively, d_{eq} is the particle volume equivalent spherical diameter and η_{K} is the Kolmogorov length scale. It has been repeatedly shown that for a sufficiently small Stokes number, the particle closely follows the fluid streamlines, without any significant deviations from the flow [34]. This, in turn, means that the relative flow velocity around a particle is low and typically falls well into the viscous (Stokes) regime. As a result, we assume a steady-state incompressible flow of a Newtonian fluid around a particle, at a very small particle Reynolds number, $\mathrm{Re_p} = ||\boldsymbol{u}||_2 d_{\mathrm{eq}}/\nu^{\mathrm{f}} \ll 1$, where $||\boldsymbol{u}||_2$ is the relative flow velocity magnitude and ν^{f} is its kinematic viscosity. In this case, the advection term in the Navier-Stokes equations can be neglected, which results in the creeping flow (Stokes) equations:

$$\boldsymbol{\nabla}\cdot\boldsymbol{u} = 0, \qquad \boldsymbol{\nabla}\cdot\boldsymbol{\sigma} + \rho^{\mathrm{f}}\boldsymbol{g} = \boldsymbol{0}. \tag{42}$$

Here $\boldsymbol{g}$ is the gravitational acceleration and $\boldsymbol{\sigma}$ is the Cauchy stress tensor defined as $\boldsymbol{\sigma} = -P\boldsymbol{i} + \boldsymbol{\tau}$, where P is the pressure, $\boldsymbol{i}$ the identity tensor, and $\boldsymbol{\tau}$ the viscous stress tensor. Considering a Newtonian fluid, we model the viscous stresses as $\tau_{ij} = \mu^{\mathrm{f}}\left[\frac{\partial u_i}{\partial x_j} + \frac{\partial u_j}{\partial x_i}\right]$, where $\mu^{\mathrm{f}} = \nu^{\mathrm{f}}\rho^{\mathrm{f}}$. Since gravity is a conservative force, which can be written as the gradient of a gravitational potential Φ, we can introduce a modified pressure as $p = P - \rho^{\mathrm{f}}\Phi$, where $\boldsymbol{g} = \boldsymbol{\nabla}\Phi$. With this, the final form of the Stokes equation reads

$$-\boldsymbol{\nabla}p + \mu^{\mathrm{f}}\boldsymbol{\nabla}^2\boldsymbol{u} = \boldsymbol{0}. \tag{43}$$

In general, the tractions on the particle boundary can now be computed using standard computational fluid dynamics (CFD) solvers, such as the Finite Volume Method (FVM), the Boundary Element Method (BEM), or other suitable numerical approaches. These methods enable evaluation of hydrodynamic forces and stresses acting on the particle surface, providing the necessary input for training our NN. As discussed in our previous work [31], for solving Stokes flow problems, the BEM offers a substantial computational advantage over the FVM (and other domain discretizing methods), primarily because the BEM requires discretization only of the boundaries rather than the entire domain. This reduction leads to significantly faster simulations, especially when large domains are required, making BEM particularly well-suited for parametric studies where a large number of simulations are necessary.

Taken together, our DNS simulations solve the boundary value problem of an ellipsoidal particle (locally) suspended in Stokes flow. In this context, we employ our open-source BEM solver (available on Zenodo [35]). Details on the BEM approach are provided in Appendix B.

3.3.2. Numerical setup

The computational domain used in the DNS study is presented in Fig. 5 and consists of a spherical domain of size D with the particle (of size d_{eq}) positioned at its center.

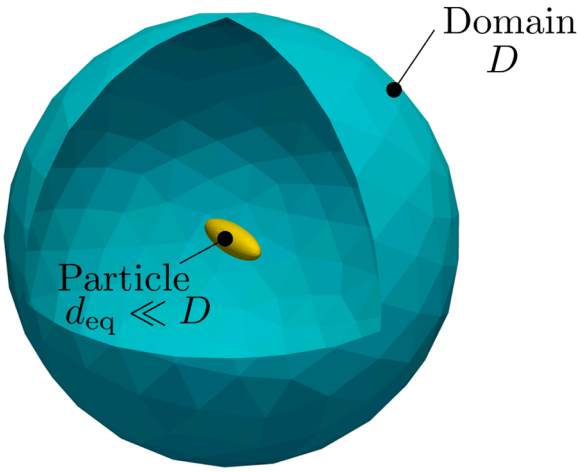

Fig. 5. Sketch of the BEM domain consisting of a spherical domain with the particle under consideration positioned in the centre of the spherical domain. The domain is of size D and the particle volume-equivalent diameter is denoted as d_{eq}. Note that the particle is scaled for display purposes. The actual size of the particle size d_{eq} is 1000 times smaller than the size of the domain D. The boundary condition on the surface of the outer sphere is a constant velocity that is prescribed in such a way that the desired velocity gradient is obtained (rotational: $\underline{l}_f^{w_1}$, $\underline{l}_f^{w_2}$, $\underline{l}_f^{w_3}$, shear: $\underline{l}_f^{d_1}$, $\underline{l}_f^{d_2}$, $\underline{l}_f^{d_3}$, expansional: $\underline{l}_f^{e_1}$, $\underline{l}_f^{e_2}$), while a no-slip condition is imposed on the particle surface.

Note that in Fig. 5 the particle size is strongly enlarged for display purposes. As reported by Štrakl et al. [36], for creeping flow around a sphere, using a domain of size $1024\, d_{\mathrm{eq}}$ reduces the influence of the domain boundaries to approximately $0.1\,\%$ compared to about $1\,\%$ achieved with the domains used in [37,38]. With this in mind, we employ a spherical domain to particle size ratio of $D/d_{\mathrm{eq}} \approx 1000$.

Dirichlet boundary conditions are imposed on both the particle surface and the outer spherical boundary of the domain. The particle velocity is set to zero, while the velocity at the outer boundary is prescribed in such a way that the desired velocity gradient is obtained. The velocity gradient is chosen such that it represents a specific flow configuration (rotational: $\underline{l}_f^{w_1}$, $\underline{l}_f^{w_2}$, $\underline{l}_f^{w_3}$, shear: $\underline{l}_f^{d_1}$, $\underline{l}_f^{d_2}$, $\underline{l}_f^{d_3}$, expansional: $\underline{l}_f^{e_1}$, $\underline{l}_f^{e_2}$). At the particle surface, a no-slip velocity boundary condition is prescribed. The boundary tractions at the particle surface are then computed by the BEM algorithm. For convenience, the simulations are set up in a non-dimensional manner ($\mu^{\mathrm{f}} = 1$, $d_{\mathrm{eq}} = 1$). To identify the form coefficients for the shear flow, the rotational flow, and the expansional flow, we require the following set of DNS studies for one specific particle shape:

- three rotational flow fields ($\underline{l}_f^{w_1}$, $\underline{l}_f^{w_2}$, $\underline{l}_f^{w_3}$),
- three shear flow fields ($\underline{l}_f^{d_1}$, $\underline{l}_f^{d_2}$, $\underline{l}_f^{d_3}$),
- two expansion flow fields ($\underline{l}_f^{e_1}$, $\underline{l}_f^{e_2}$).

Taken together, this adds up to a total of $8 = 3 + 3 + 2$ simulations for each selected particle shape to determine all relevant form coefficients.

3.3.3. Mesh study and validation

To validate the proposed algorithm and assess its accuracy, we first examine an ellipsoidal particle, varying the axial ratio λ_1. Recall that for ellipsoids, Jeffery [7] analytically derived the tractions on the particle surface under creeping flow conditions. Ravnik et al. [39] later showed that these expressions are only valid for particles whose size is much smaller than the Kolmogorov length scale η_K. The specific formulas for the traction, as originally provided by Jeffery [7], are detailed in Section 2.1. In the following, we investigate a spherical particle ($\lambda_1 = 1$, $\lambda_2 = 1$) and three prolate particles ($\lambda_1 = 2.5$, $\lambda_1 = 5$ and $\lambda_2 = 7.5$).

It is important to note that particle surface discretization (as discussed in the following) is only required to obtain the traction results to train the NN, i.e., in the offline phase. The online calculation of the particle deformation is meshless and thus highly efficient. In the offline calculation, the domain discretization is carried out in two steps. First, the outer boundary of the domain (the outer sphere) is meshed separately, using approximately 300 elements – this remains constant across all cases. The particle surface itself is then meshed, with four different mesh settings, which result in the mesh statistics as presented in Table 1. Note that the meshing procedure is automated and consists of an in-house Python STL generator, a subsequent remeshing step in OpenFOAM (blockMesh, snappyHexMesh), followed by a conversion to Gmsh, which can then be employed in the in-house BEM code. In OpenFOAM, the different meshes are generated by employing an identical background mesh, where the number of background mesh elements is refined with a coefficient of $2^{1/3}$ for each increasing MeshID. Furthermore, we employ an increased refinement level at mesh regions, where the angle between adjacent local surface normals exceeds $60°$. This enables a refinement of strong surface gradients, which is especially relevant for strongly elongated and oblate particles.

Table 1
Particle surface mesh statistics: Number of elements per particle surface for each investigated MeshID.

Shape / MeshID		0	1	2	3
$\lambda_1 = 1$	$\lambda_2 = 1$	278	486	822	1218
$\lambda_1 = 2.5$	$\lambda_2 = 1$	382	514	834	1338
$\lambda_1 = 5$	$\lambda_2 = 1$	822	826	1698	1722
$\lambda_1 = 7.5$	$\lambda_2 = 1$	806	996	1420	2002

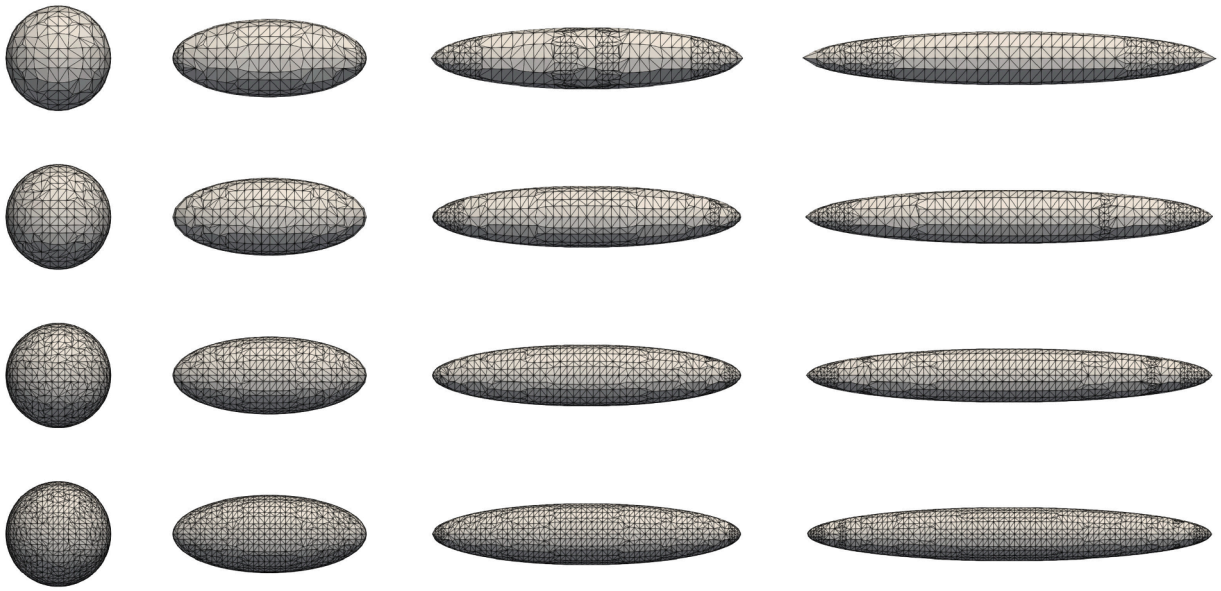

Fig. 6. Resulting surface meshes for a spherical particle and three prolate particles ($\lambda_2 = 2.5,\ 5,\ 7.5$ from left to right). MeshIDs from top to bottom: 0,1,2,3.

As presented in Table 1, the number of particle surface elements strongly depends on the particle shape under consideration. We find that oblate particles, in general, result in a larger number of surface elements than their prolate counterparts. This is due to the larger surface area of an oblate ellipsoid compared to a prolate ellipsoid with identical λ_1. Taken together, the number of elements increases with increasing aspect ratio and increasing MeshID. Exemplarily, the resulting meshes for the spherical particle and three prolate particles ($\lambda_2 = 2.5,\ 5,\ 7.5$) are displayed in Fig. 6.

To choose an appropriate mesh resolution, we compare the resulting DNS traction for a certain MeshID to the analytically obtained tractions, as given by Jeffery [7]. This is done by employing the normalized error $\hat{E}$, which is obtained for expansional, shear, and rotational form coefficients as follows

$$\hat{E}_i^e = \frac{|\hat{f}_{i\,\mathrm{DNS}}^e - \hat{f}_i^e|}{\sqrt{\sum_{i=1}^{3} \left[\hat{f}_i^e\right]^2}}, \quad \hat{E}_i^w = \frac{|\hat{f}_{i\,\mathrm{DNS}}^w - \hat{f}_i^w|}{\sqrt{\sum_{i=1}^{2} \left[\hat{f}_i^w\right]^2}}, \quad \hat{E}_i^d = \frac{|\hat{f}_{i\,\mathrm{DNS}}^d - \hat{f}_i^d|}{\sqrt{\sum_{i=1}^{2} \left[\hat{f}_i^d\right]^2}} \tag{44}$$

where $\hat{f}_{i\,\mathrm{DNS}}^e$ $\hat{f}_{i\,\mathrm{DNS}}^w$ and $\hat{f}_{i\,\mathrm{DNS}}^d$ represent the DNS form coefficients and $\hat{f}_i^e$ $\hat{f}_i^w$ and $\hat{f}_i^d$ represent the corresponding analytical values. Note that each rotational and shear flow configuration yields two form coefficients, whereas each expansional flow configuration yields three form coefficients.

Observe that the numerator (i.e. $|\hat{f}_{i\,\mathrm{DNS}}^e - \hat{f}_i^e|$) in Eq. (44) represents the absolute error between the predicted and analytical values. The denominator ($\sqrt{\dots}$) normalizes the absolute error by computing the Euclidean norm (magnitude) of the traction tensor, ensuring that the errors are scaled relative to the overall magnitude of the obtained traction tensor. This normalization provides a fair comparison as it ensures that the errors are interpreted in a way that considers the overall scale of the traction tensor for each respective flow configuration. Table 2 presents the accuracy of the DNS simulation for the four different meshes (see Table 1) by providing the average $\bar{E}$ for shear-flow ($\bar{E}^d$), rotational-flow ($\bar{E}^w$) and expansional flow $\hat{\bar{E}}^e$), which are obtained using

$$\begin{aligned} \bar{E}^w &= \left[\hat{E}_1^w + \hat{E}_2^w + \hat{E}_3^w\right]/3 \\ \bar{E}^d &= \left[\hat{E}_1^d + \hat{E}_2^d + \hat{E}_3^d\right]/3 \\ \bar{E}^e &= \left[\hat{E}_1^e + \hat{E}_2^e\right]/2\,. \end{aligned} \tag{45}$$

Table 2
Mesh study: Resulting deviation ([%]) between the DNS form coefficients and the analytical form coefficients. The error is evaluated as the mean of the specific flow configurations, i.e., shear-flow ($\bar{E}^d$), rotational-flow ($\bar{E}^w$), and expansional flow ($\bar{E}^e$) for each MeshID (MID).

Shape		$\lambda_1 = 1,\ \lambda_2 = 1$			$\lambda_1 = 2.5,\ \lambda_2 = 1$			$\lambda_1 = 5,\ \lambda_2 = 1$			$\lambda_1 = 7.5,\ \lambda_2 = 1$		
Error [%]		$\bar{E}^w$	$\bar{E}^d$	$\bar{E}^e$	$\bar{E}^w$	$\bar{E}^d$	$\bar{E}^e$	$\bar{E}^w$	$\bar{E}^d$	$\bar{E}^e$	$\bar{E}^w$	$\bar{E}^d$	$\bar{E}^e$
MID	0	2.20	2.20	1.71	1.73	1.83	1.64	1.55	1.58	1.49	1.60	1.47	0.98
	1	1.33	1.31	1.04	1.67	1.701	1.34	1.26	1.30	1.10	1.37	1.29	0.97
	2	0.83	0.81	0.66	1.06	1.09	0.928	0.93	0.94	0.92	0.99	0.96	0.77
	3	0.58	0.57	0.45	0.68	0.70	0.70	0.74	0.75	0.84	0.70	0.69	0.67

As observed, the error in predicting the form coefficients decreases with increasing mesh refinement. Furthermore, we find that M2 and M3 mesh consistently provide errors of $\approx 1\,\%$. Consequently, we employ the M2 mesh discretization for particles up to $\lambda_1 = 7.5$, and for particles with $\lambda_1 > 7.5$, we employ the finer M3 mesh discretization.

4. Neural network for modeling soft particles in flows

To model flow-induced deformations of soft particles of more complex particle shapes, in the following, we present a neural network architecture designed to predict the form coefficients of the traction exerted on a micro-particle suspended in viscous flows (locally Stokes flow). In this work, we employ a neural network rather than polynomial fitting (as used in Štrakl et al. [36]). Polynomial regression becomes increasingly impractical when dealing with multiple outputs and complex nonlinear relationships, as higher-order models suffer from numerical instability, oscillatory behavior, and overfitting tendencies [40]. Although it can capture simple trends, polynomial fitting is highly sensitive to noise and lacks flexibility when approximating irregular or non-smooth functions [41]. Neural networks provide a more suitable alternative: they naturally map a small number of inputs to many outputs without requiring separate models or complex multivariate expansions [41], and they are universal function approximators capable of capturing nonlinear dependencies without explicitly defined basis functions [42]. Since our training data also originates from DNS simulations, which may include mesh-induced irregularities, the generalization ability of neural networks makes them more robust to noise than polynomial models [43]. For these reasons, we adopt a neural network to capture both analytical and DNS-derived data in a compact and generalizable form.

The data feeding the neural networks can be generated in two ways:

- (a) using analytical expressions (only available for a limited number of shapes such as spheres and ellipsoids),
- (b) using dedicated DNS simulations.

For the problem under consideration, the inputs are given by the particle shape parameters λ_1 and λ_2, while the outputs correspond to the form coefficients associated with each flow field contribution (expansional, rotational, and shear). These coefficients quantify the scaling of the respective flow field influences on the resulting tractions. The number of traction form coefficients depends on the current chosen flow field configuration. In the case of an expansional flow configuration, we have to determine three form coefficients; for the shear and rotational flow configurations, we require only two for each.

In the context of this study, we found that a NN model consisting of an input layer with 2 neurons (λ_1, λ_2), followed by four fully connected hidden layers with 8, 8, 8, and 6 neurons, respectively, proved to be sufficient. Furthermore, we employ the Tanh activation function for the first three hidden layers and the Sigmoid activation function for the fourth hidden layer to introduce non-linearity and improve learning dynamics. The output layer comprises either two (for shear and rotational flow fields) or three (for expansional flow fields) neurons without bias, reflecting the final prediction targets. The employed NN architecture is sketched in Fig. 7. The network is trained using the AdamW optimizer with a learning rate of 0.01, and a learning rate scheduler is applied to reduce the learning rate by a coefficient of 0.90 every 1000 steps. For a NN that is supposed to perform regression, the Mean Squared Error (MSE) of the predicted output with respect to the expected value is a common loss function choice [44]. It computes the average squared difference between the predicted values and the target values. Given that the network has three output neurons (as in the case of expansional flow), the loss function based on the MSE is defined as

$$L = \frac{1}{N_p}\sum_{i=1}^{N_p}\left[\hat{f}_{i,1} - \hat{f}^*_{i,1}\right]^2 + \left[\hat{f}_{i,2} - \hat{f}^*_{i,2}\right]^2 + \left[\hat{f}_{i,3} - \hat{f}^*_{i,3}\right]^2, \tag{46}$$

where

- $\hat{f}_{i,1}, \hat{f}_{i,2}, \hat{f}_{i,3}$ are the predicted outputs of the neural network for the ith input sample, corresponding to the three (or two) output neurons.
- $\hat{f}^*_{i,1}, \hat{f}^*_{i,2}, \hat{f}^*_{i,3}$ are the reference or target values for the ith input sample, corresponding to the three (or two) output neurons.

Fig. 7 sketches the effective total NN structure to predict all form coefficients necessary to model the tractions exerted on a soft micro-particle (locally) suspended in Stokes flows. Observe that our NN does not explicitly impose physics-based constraints.

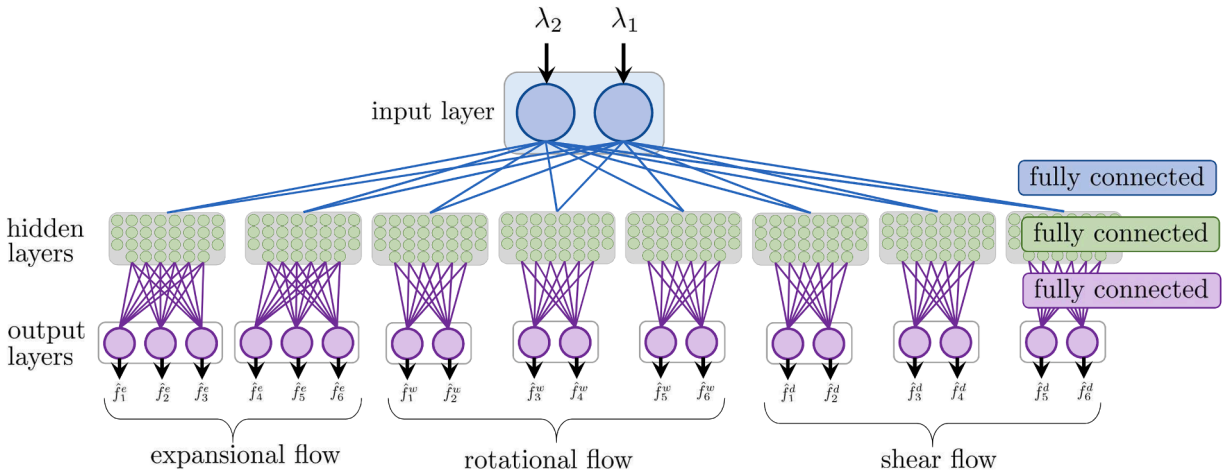

Fig. 7. Structure of the employed fully connected neural network model consisting of two input neurons, 4 hidden layers of size $8 \times 8 \times 8 \times 6$ and three output neurons for each considered expansional flow configuration and two output neurons for each shear and rotational flow configuration. For the problem under consideration, the inputs are given by the particle shape parameters λ_1 and λ_2, while the outputs correspond to the form coefficients associated with each flow field contribution (expansional, rotational, and shear). These coefficients quantify the scaling of the respective flow field influences on the resulting tractions.

However, the construction of the shape factors (as described in Section 3) inherently incorporates key physical properties such as symmetry and related invariances. Since the neural network operates on these derived factors, it cannot violate these constraints. In this way, the physics-awareness is embedded indirectly through the choice of input representation.

The k-fold cross-validation is particularly useful when a precise and robust model is required. This technique involves performing cross-validation k times while shuffling the data before each split. The final performance score is obtained by averaging the results of all iterations. In the scope of this study, we employ $k = 10$. The k-fold cross-validation allows to evaluate the model variance, which is a measure of the spread of the accuracy of the obtained NN. It also shows how strongly the NN accuracy depends on the training dataset (10 % of the total dataset) that was randomly selected, as it indicates how far the specific model errors deviate from the mean model error. The model error variance is obtained using

$$\sigma_\epsilon^2 = \frac{1}{k} \sum_{i=1}^{k} \left[L_i - \mu \right]^2 \tag{47}$$

with mean μ

$$\mu = \frac{1}{k} \sum_{i=1}^{k} L_i \,. \tag{48}$$

4.1. Neural network from analytical results

To start with, a NN is trained from the analytical form coefficients as presented in Eqs. (25),(28),(35) in combination with the $\alpha_0,\ \beta_0,\ \gamma_0$ obtained as described in Eq. (15) for ellipsoidal particles. Using this expression, a dataset of form coefficients can be obtained. In the following, we investigate the form coefficients in a range of $\lambda_1 \in [1,\ 10]$ and $\lambda_2 \in \left[1,\ \lambda_1\right]$ using three different dataset sizes:

- I.: $\Delta\lambda_i = 0.01$ leading to $406,351$ analytical data points to train the NN.
- II.: 10 % of dataset I. leading to $40,635$ analytical data points to train the NN.
- III.: 1 % of dataset I. leading to 4063 analytical data points to train the NN.
- IV.: 0.1 % of dataset I. leading to 406 analytical data points to train the NN.

The accuracy of the NN for rotational flow, shear flow, and expansional flow form coefficients is presented for each dataset using a k-fold test, where we select $k = 10$.

First, the minimum and average prediction errors (MSE), along with the error variance, are reported for the NN tasked with estimating form coefficients of rotational flow. These results are summarized in Table 3. As shown in Table 3, the average error across the k-fold evaluation for the coarsest dataset with 406 data points (IV.) in the case of rotational form coefficients is $\bar{\epsilon} \leq 1.2 \times 10^{-6}$, with an error variance of $\sigma_\epsilon \leq 2.4 \times 10^{-12}$. For the next finer dataset with 4063 samples (III.), the mean error improves by nearly an order of magnitude to $\bar{\epsilon} \leq 1.3 \times 10^{-7}$, with a variance of $\sigma_\epsilon \leq 3.5 \times 10^{-14}$. Increasing the dataset size further to 40635 samples (II.) and 406351 samples (I.) yields only slight improvements, with the differences between these finest cases being minimal. This indicates

Table 3
Neural network error metrics of form coefficients for rotational flow for four different dataset sizes ($I. - IV.$). The table presents the minimum MSE ($\epsilon_{\min}$), mean MSE ($\bar{\epsilon}$), and error variance (σ_ϵ) of the k-fold test with $k = 10$. Note that $\bar{f}^w$ represents the mean error of all $\hat{f}_i^w$.

Metric		$\hat{f}_1^w, \hat{f}_2^w$	$\hat{f}_3^w, \hat{f}_4^w$	$\hat{f}_5^w, \hat{f}_6^w$	$\bar{f}^w$
	$\epsilon_{\min}$	3.3186e-08	2.6216e-08	2.7518e-08	2.8973e-08
I.	$\bar{\epsilon}$	9.1919e-08	6.0399e-08	8.2552e-08	7.829e-08
	σ_ϵ	2.1895e-15	4.8498e-16	3.5733e-15	2.0826e-15
	$\epsilon_{\min}$	4.8006e-08	2.7762e-08	1.9432e-08	3.1733e-08
II.	$\bar{\epsilon}$	8.9313e-08	7.3717e-08	8.0856e-08	8.1295e-08
	σ_ϵ	2.2644e-15	2.1564e-15	1.3389e-15	1.9199e-15
	$\epsilon_{\min}$	4.5151e-08	2.5106e-08	4.4917e-08	3.8391e-08
III.	$\bar{\epsilon}$	1.1222e-07	7.3494e-08	2.1723e-07	1.3431e-07
	σ_ϵ	2.2799e-15	1.0979e-15	1.0302e-13	3.5466e-14
	$\epsilon_{\min}$	1.053684e-07	7.501887e-08	2.024393e-07	1.2761e-07
IV.	$\bar{\epsilon}$	1.731615e-07	2.125942e-06	1.393763e-06	1.2310e-06
	σ_ϵ	1.591975e-15	3.16152e-12	3.962276e-12	2.3751e-12

Table 4
Neural network error metrics of form coefficients for shear flow for four different dataset sizes ($I. - IV.$). The table presents the minimum MSE ($\epsilon_{\min}$), mean MSE ($\bar{\epsilon}$), and error variance (σ_ϵ) of the k-fold test with $k = 10$. Note that $\bar{f}^d$ represents the mean error of all $\hat{f}_i^d$.

Metric		$\hat{f}_1^d, \hat{f}_2^d$	$\hat{f}_3^d, \hat{f}_4^d$	$\hat{f}_5^d, \hat{f}_6^d$	$\bar{f}^d$
	$\epsilon_{\min}$	4.9401e-08	2.9036e-08	3.2981e-08	3.7139e-08
I.	$\bar{\epsilon}$	1.138e-07	9.4287e-08	6.3643e-08	9.0577e-08
	σ_ϵ	3.5266e-15	4.3602e-15	7.0244e-16	2.8631e-15
	$\epsilon_{\min}$	3.96e-08	3.2743e-08	2.9124e-08	3.3822e-08
II.	$\bar{\epsilon}$	1.015e-07	1.0143e-07	6.705e-08	8.9993e-08
	σ_ϵ	2.3293e-15	1.9793e-14	8.1258e-16	7.645e-15
	$\epsilon_{\min}$	3.5256e-08	3.9858e-08	1.9224e-08	3.1446e-08
III.	$\bar{\epsilon}$	9.1839e-08	1.7298e-07	1.7471e-07	1.4651e-07
	σ_ϵ	1.4394e-15	9.3606e-14	6.304e-14	5.2695e-14
	$\epsilon_{\min}$	2.235097e-07	9.058544e-07	1.967025e-07	4.4202e-07
IV.	$\bar{\epsilon}$	7.51529e-07	1.2138616e-06	4.397814e-07	8.0172e-07
	σ_ϵ	7.107199e-13	7.920558e-14	3.068257e-14	2.7354e-13

that dataset $III.$ already provides sufficiently accurate performance of the neural network for rotational form coefficients, and further increasing the number of training samples leads to only diminishing improvement.

Second, the NN trained to predict the form coefficients for shear flow is analyzed. The minimum and average prediction errors, as well as the error variances across the k-fold evaluation, are summarized in Table 4. Once again, the results demonstrate that the overall prediction accuracy is high for datasets I.-III., with average errors consistently on the order of 1×10^{-7} to 9×10^{-8}. Importantly, we observe that the dataset III. (4063 samples) already yields sufficiently small errors, with only minor deviations when compared to the larger datasets, i.e., II. (40,635 samples) and I. (406,350 samples). This indicates that further enlarging the dataset beyond III. does not significantly improve the predictive capability of the NN. By contrast, we find that the dataset IV. (406 samples) exhibits a substantially larger mean error and variance ($\bar{\epsilon} \approx 8 \times 10^{-7}$ and $\sigma_\epsilon \approx 3 \times 10^{-13}$) compared to III. ($\bar{\epsilon} \approx 1.5 \times 10^{-7}$ and $\sigma_\epsilon \approx 5 \times 10^{-14}$), underlining that this sample size (IV.) might be insufficient to achieve reliable accuracy. Taken together, the results indicate that a dataset size of 4063 samples is sufficient to train the NN for predicting the form coefficients in shear flow.

Third, the NN tasked with predicting form coefficients of expansional flow is discussed. The corresponding minimum and average prediction errors, along with the error variance, are summarized in Table 5. We observe that the average error across the k-fold evaluation is slightly higher for all data sets compared to the shear and rotational flow form coefficients. Nevertheless, they remain sufficiently low for all studied datasets to confirm the robustness of the NN in accurately predicting the shear flow form coefficients.

Fig. 8 presents the parity plots illustrating the correspondence between the NN's predicted values (NN with the minimum error) and the true (analytical) form coefficients for the selected training dataset ($III.$). Ideally, the predictions would lie along the diagonal, indicating agreement between the model outputs and the analytical data. As displayed in Fig. 8 (a–c), we observe a close alignment of data points along the diagonal, for all flow field configurations studied, indicating high predictive accuracy of the NN. Furthermore, we observe a clear difference in the magnitude of the form coefficients, which are presented using different colors.

Table 5
Neural network error metrics of form coefficients for expansional flow for four different dataset sizes ($I. - IV.$). The table presents the minimum MSE ($\epsilon_{\min}$), mean MSE ($\bar{\epsilon}$), and error variance (σ_ϵ) of the k-fold test with $k = 10$. Note that $\bar{f}^e$ represents the mean error of all $\hat{f}_i^e$.

Metric		$\hat{f}_1^e, \hat{f}_2^e, \hat{f}_3^e$	$\hat{f}_4^e, \hat{f}_5^e, \hat{f}_6^e$	$\bar{f}^e$
I.	$\epsilon_{\min}$	6.89e-08	7.93e-08	7.41e-08
	$\bar{\epsilon}$	1.076e-07	1.358e-07	1.217e-07
	σ_ϵ	1.1295e-15	3.8656e-15	2.4976e-15
II.	$\epsilon_{\min}$	8.13e-08	8.44e-08	8.285e-08
	$\bar{\epsilon}$	1.444e-07	1.262e-07	1.353e-07
	σ_ϵ	3.9824e-15	1.3538e-15	2.6681e-15
III.	$\epsilon_{\min}$	8.81e-08	5.8e-08	7.305e-08
	$\bar{\epsilon}$	8.797e-07	3.021e-07	5.909e-07
	σ_ϵ	1.6199e-12	1.8005e-13	8.9998e-13
IV.	$\epsilon_{\min}$	4.352472e-07	2.488161e-07	3.4203e-07
	$\bar{\epsilon}$	1.717383e-06	5.038082e-07	1.1106e-06
	σ_ϵ	2.943573e-12	4.295154e-14	1.4933e-12

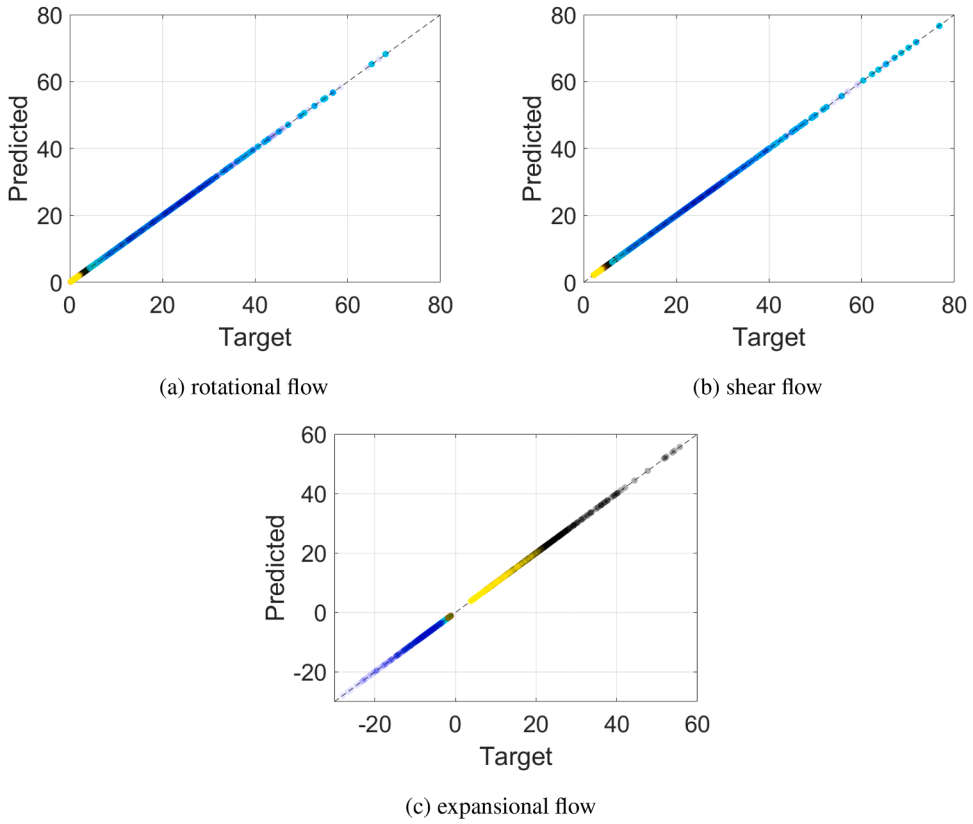

(a) rotational flow

(b) shear flow

(c) expansional flow

Fig. 8. NN prediction accuracy for form coefficients for different flow field configurations ((a), (b), and (c)). The predicted values are displayed over the analytically obtained target values. Form coefficients: ● $\hat{f}_1^\alpha$ ● $\hat{f}_2^\alpha$ ● $\hat{f}_3^\alpha$ ● $\hat{f}_4^\alpha$ ● $\hat{f}_5^\alpha$ ● $\hat{f}_6^\alpha$ with $\alpha = w, d, e$.

4.2. Neural network from DNS simulations

Next, a NN is derived from the form coefficients obtained using direct numerical simulations (DNS), specifically by solving the boundary value problem for an ellipsoidal particle suspended in a locally Stokesian flow by BEM. Using the simulation results for the eight different flow configurations (3x shear, 3x rotational, 2x expansional flow), a dataset of form coefficients can be constructed. The shape space is discretized in the range of $\lambda_1 \in [1,\ 10]$ and $\lambda_2 \in \left[1,\ \lambda_1\right]$ with $\Delta\lambda = 0.1$, leading to 4186 data points to train the NN.

Table 6
Neural network error metrics of form coefficients for rotational flow obtained from DNS data.

Rotational	$\hat{f}_1^w, \hat{f}_2^w$	$\hat{f}_3^w, \hat{f}_4^w$	$\hat{f}_5^w, \hat{f}_6^w$
$\epsilon_{\min}$	3.32e-07	4.07e-07	6.39e-07
$\bar{\epsilon}$	4.26e-07	6.88e-07	7.43e-07
σ_ϵ	4.21e-15	3.46e-15	5.22e-15

Table 7
Neural network error metrics of form coefficients for shear flow obtained from DNS data.

Shear	$\hat{f}_1^d, \hat{f}_2^d$	$\hat{f}_3^d, \hat{f}_4^d$	$\hat{f}_5^d, \hat{f}_6^d$
$\epsilon_{\min}$	3.89e-07	1.54e-06	2.03e-06
$\bar{\epsilon}$	4.70e-07	1.82e-06	2.23e-06
σ_ϵ	1.9e-15	2.72e-14	3.08e-14

Table 8
Neural network error metrics of form coefficients for expansional flow obtained from DNS data.

Expansional	$\hat{f}_1^e, \hat{f}_2^e, \hat{f}_3^e$	$\hat{f}_4^e, \hat{f}_5^e, \hat{f}_6^e$
$\epsilon_{\min}$	1.59e-05	2.84e-05
$\bar{\epsilon}$	2.11e-05	4.69e-05
σ_ϵ	8.07e-12	1.06e-10

The NN architecture remains identical to the setup used with analytical data: it consists of two input neurons ($\lambda_1,\ \lambda_2$), four fully connected layers with 8, 8, 8, and 6 neurons, and an output layer comprising either 2 neurons for shear and rotational flow, or 3 neurons for expansional flow.

Note that when training the NN using form coefficients obtained from DNS instead of analytical data, we observe a slight increase in prediction error, see Tables 6–8. While the overall average errors remain very small and well within acceptable limits, the most pronounced increase occurs in the prediction of the form coefficients for expansional flow (see Table 8). In contrast, the errors associated with shear and rotational flow parameters (see Tables 6 and 7) show only a marginal increase. These results suggest that, although switching from analytical to DNS data (as required for particles without available analytical traction expressions) introduces some additional deviations due to mesh discretization and numerical accuracy, the NN still maintains high predictive accuracy across all flow types as shown in Fig. 9. Consequently, the proposed approach for predicting surface tractions proves effective and can be confidently applied to develop NN models for simulating soft as well as rigid particles suspended in flows.

5. Demonstrative examples

In the following, we validate our NN approach to model soft deformable particles in flows by comparing it to numerical studies from the literature for soft initially spherical and ellipsoidal particles. Throughout the demonstrative examples (unless explicitly stated otherwise), the characteristic scales for nondimensionalization are the length scale d_{eq} (initial volume-equivalent particle diameter), the time scale $\dot{\gamma}^{-1}$ (inverse fluid shear-rate) and the fluid pressure/stress scale $\mu^{\text{f}}\dot{\gamma}$. Here, μ^{f} denotes the dynamic viscosity of the fluid. In the following, we use the Capillary number Ca to quantify the softness of the particle, which represents the ratio of the viscous forces in the fluid to the elastic forces in the particle, [26] as

$$\text{Ca} = \frac{\mu^{\text{f}}\dot{\gamma}}{\mu^{\text{s}}}, \tag{49}$$

with μ^{s} denoting the particle shear modulus. Note that a larger Capillary number Ca is associated with a softer particle [26]. Furthermore, we can define the particle shear Reynolds number using the fluid shear rate $\dot{\gamma}$ as

$$\text{Re}_{\dot{\gamma}} = \frac{\dot{\gamma}\, d_{\text{eq}}^2}{\nu^{\text{f}}}, \tag{50}$$

where ν^{f} denotes the kinematic viscosity of the fluid. Note that a key assumption of the Jeffery-Roscoe solution is creeping flow with $\text{Re}_{\dot{\gamma}} \ll 1$ locally.

To characterize the deformation of the particles, we introduce the Taylor deformation parameter $\hat{\ell}$, which serves as a standard measure of droplet and vesicle deformation, as noted by Stone et al., [45]. The deformation parameter can be expressed in terms of

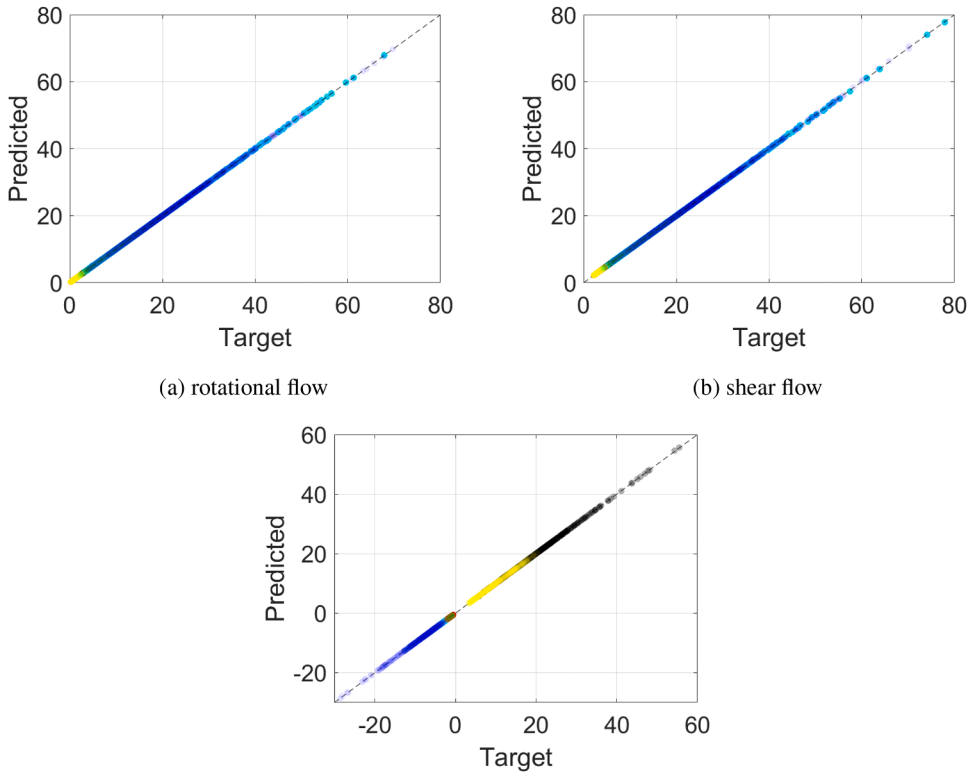

(a) rotational flow

(b) shear flow

(c) expansional flow

Fig. 9. NN prediction accuracy for form coefficients for different flow field configurations ((a) (b) and (c)). The predicted value is displayed over the (DNS) target value. Form coefficients: ● $\hat{f}_1^{\alpha}$ ● $\hat{f}_2^{\alpha}$ ● $\hat{f}_3^{\alpha}$ ● $\hat{f}_4^{\alpha}$ ● $\hat{f}_5^{\alpha}$ ● $\hat{f}_6^{\alpha}$ with $\alpha = w, d, e$.

the semi-axis ratios of the particle, using $\ell_1 = a_2/a_1$ and $\ell_2 = a_3/a_1$ (recall that $a_3 \leq a_2 \leq a_1$), as [26]

$$\hat{\ell} = \frac{a_1 - a_2}{a_1 + a_2} = \frac{1 - \ell_1}{1 + \ell_2}\,. \tag{51}$$

According to Gao et al., [26], for less soft particles, i.e. $\hat{\ell} < 0.2$, one can assume a linear relation between $\hat{\ell}$ and Ca ($\hat{\ell} \approx \mathrm{Ca}$). However, as the particles exhibit increased softness (Ca ↗), a non-linear relationship exists between Ca and $\hat{\ell}$, [26]. In the limit $\mathrm{Ca} \to \infty$, the elastic shear modulus μ^{s} becomes negligible compared to the viscous stresses, and the particle deforms without elastic resistance. In this regime, $\hat{\ell}$ approaches 1, corresponding to the extreme case where the major axis a_1 extends infinitely larger than the minor axis a_2. Thus, $\hat{\ell} = 1$ represents an "infinitely soft" particle, i.e., a body that offers no resistance to elongation and behaves as a super-soft entity, consistent with the observations in Gao et al. [26].

In addition, the Stokes number, which is defined as the ratio of the characteristic particle response time τ^{s} to a characteristic time of the flow τ^{f}, for a particle with volume equivalent sphere diameter d_{eq}, reads as

$$\mathrm{Stk} = \frac{\tau^{\mathrm{s}}}{\tau^{\mathrm{f}}} = \frac{\rho^{\mathrm{s}}}{\rho^{\mathrm{f}}} \frac{\mathrm{d}_{\mathrm{eq}}^2 \mathrm{U}}{18\nu^{\mathrm{f}} \mathrm{L}}\,. \tag{52}$$

with the characteristic time scales defined as follows:

$$\tau^{\mathrm{s}} = \frac{\rho^{\mathrm{s}}}{\rho^{\mathrm{f}}} \frac{d_{\mathrm{eq}}^2}{18\nu^{\mathrm{f}}}, \quad \tau^{\mathrm{f}} = \frac{L}{U}, \tag{53}$$

where L and U denote a characteristic length and velocity of the flow problem, respectively. Note that we neglect the pressure gradient and added mass force as we assume that $\rho^{\mathrm{s}} \gg \rho^{\mathrm{f}}$ and/or $\mathrm{Stk} \ll 1$.

5.1. Quasi-rigid body limit

As a first demonstrative example, we investigate prolate ellipsoids suspended in a laminar pipe flow. The setup is consistent with the setup employed in Wedel et al. [19], which builds upon the study by Tian et al. [46]. The circular channel has diameter of $D = 4.2\,\mathrm{mm}$ and a mean velocity of $\bar{u} = 0.485\ \mathrm{m/s}$ [19]. The studied prolate ellipsoids have an aspect ratio of $\lambda_1 = 1.5,\ 3,\ 7$, with a semi-minor axis of $a_3 = 0.5\,\mu\mathrm{m}$ and density of $\rho^{\mathrm{s}} = 2560\,\mathrm{kg/m^3}$. The fluid density is set to $\rho^{\mathrm{f}} = 1.208\,\mathrm{kg/m^3}$, and the kinematic viscosity is

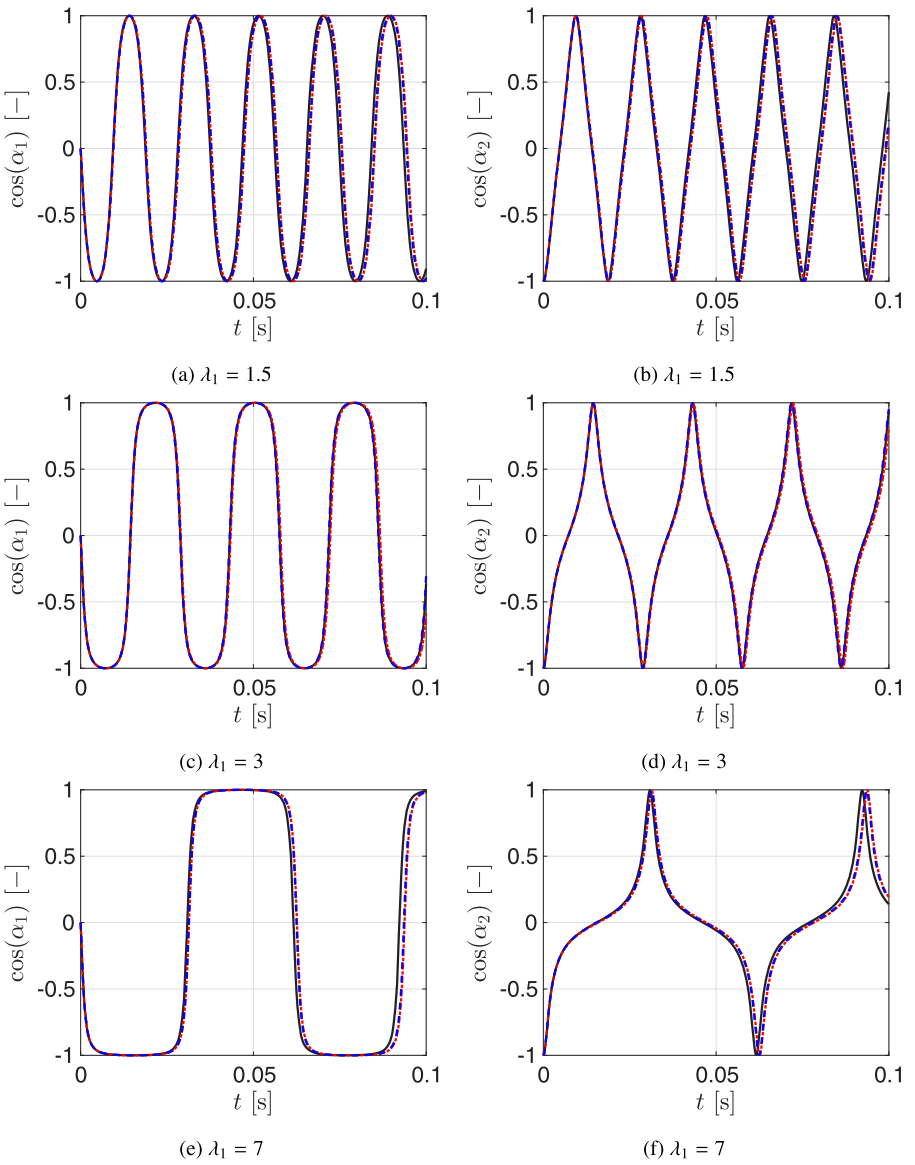

(a) $\lambda_1 = 1.5$ (b) $\lambda_1 = 1.5$

(c) $\lambda_1 = 3$ (d) $\lambda_1 = 3$

(e) $\lambda_1 = 7$ (f) $\lambda_1 = 7$

Fig. 10. Direction cosines $\cos(\alpha_1)$ and $\cos(\alpha_2)$ of the particle long axis with the streamwise and gravitational direction, respectively. The considered prolate ellipsoids possess $\lambda_1 = 1.5,\ 3,\ 7$ and are suspended in a laminar pipe flow. Displayed data: Wedel et al. [19], present model (NN-An.), present model (NN-DNS).

$\nu^{\mathrm{f}} = 1.491 \times 10^{-5}\,\mathrm{m}^2/\mathrm{s}$, resulting in a Reynolds number of $\mathrm{Re} = 137$. Notably, $\rho^{\mathrm{s}} \gg \rho^{\mathrm{f}}$. Additionally, the characteristic particle response time is $\tau^{\mathrm{s}} = 0.046\,\mathrm{ms}$, which corresponds to a Stokes number of $\mathrm{Stk} = 0.01$. The particle is initially positioned at $x_2(0) = -1.65\,\mathrm{mm}$ in the $\boldsymbol{e}_1 - \boldsymbol{e}_2$ plane, with an initial orientation of $\phi_1 = -90°,\ \phi_2 = 0°,\ \phi_3 = 0°$, and initial velocity and angular velocity set to zero. At the initial position $\underline{x}(0)$, the flow vorticity is $\omega_{\mathrm{f}} = 726\,\mathrm{s}^{-1}$.

In this study, we investigate the novel soft particle tracking model in the rigid particles limit by choosing $\mathrm{Ca} \to 0$. In the following, we compare the direction cosines of the particle's long axis with the streamwise and gravitational direction for prolate ellipsoids with aspect ratios $\lambda_1 = 1.5,\ 3$, and 7 suspended in laminar pipe flow. Results for rigid particles (see Wedel et al. [19]) are contrasted with those for quasi-rigid particles, obtained using the NN trained either on analytical or on DNS data.

Fig. 10 shows time series comparisons of direction cosines with the streamwise ($\cos(\alpha_1)$) and gravitational ($\cos(\alpha_2)$) direction for different values of λ_1, illustrating the accuracy of the NN models in the limit of $\mathrm{Ca} \to 0$ (quasi-rigid). For $\lambda_1 = 1.5$ (a,b), the results demonstrate excellent agreement between the reference and computed solutions. Similarly, for $\lambda_1 = 3$ (c,d), the match remains highly accurate, maintaining close alignment throughout the time window. Also for increased elongated particles, i.e. $\lambda_1 = 7$ (e,f), only minor discrepancies arise, indicating the robustness and fidelity of the approach across a range of ellipsoidal particles. Consequently, we consider the novel NN soft particle tracking model validated in the limit of $\mathrm{Ca} \to 0$.

5.2. Shape dynamics of soft spherical particles in simple shear flow

The next validation step involves the study of an elastic (neo-Hookean) initially spherical particle suspended in a simple shear flow ($l_{f\,12} = \dot{\gamma}$). Note that the fluid rate of deformation tensor $\boldsymbol{d}_f$ has two non-zero components, $d_{21} = d_{21}$, likewise to the fluid vorticity $w_{21} = -w_{21}$. As a reference, we draw on the results of Gao et al., [26], who studied soft initially spherical particles subject to simple shear flow. As the authors report, they achieved excellent agreement with the reported results of Roscoe [24]. However, to achieve comparability with the study of Roscoe, Gao et al. neglected the viscous contribution present in Roscoe's solution.

5.2.1. Steady-state particle deformation

Initially, we investigate the steady-state results of the particle deformation, i.e. the Taylor deformation parameter $\hat{\ell}$, the particle half axis ratio parameters ℓ_1, ℓ_2, and the particle orientation ϕ. As presented in Fig. 11 (a,b), both NN approaches (NN-DNS, NN-An.) are able to excellently reproduce the steady-state particle deformation parameter $\hat{\ell}$ as well as the particle half axis ratio parameters ℓ_1, ℓ_2 as reported by Gao et al., [24]. Observe that no notable discrepancies between NN-DNS and NN-An. are observed, indicating that the DNS approach to model the tractions exerted on the particle surface is sufficiently accurate.

Next, we examine the steady-state orientation of the particle, as shown in Fig. 12. The results demonstrate that the proposed NN models accurately capture the steady-state orientation reported by Gao et al. [26], achieving excellent agreement. Again the deviations between NN-DNS and NN-An. are negligible.

It is known that initially spherical soft particles suspended in simple shear flow experience the so-called tank-treading dynamics [26,47]. Tank-treading motion is characterized by a soft particle maintaining a steady-state shape and orientation while its material continues to deform. Consequently, we can analyse the relation between particle softness (Ca) and the material spin tensor $\boldsymbol{w}_s$, i.e. the tank-treading frequency. Fig. 12 (b) illustrates this relationship. As observed, we obtain in the quasi-rigid particle limit (Ca $\to$ 0), a tank-treading frequency equal to half the flow vorticity ($\dot{\gamma}/2$). As particle deformability increases, a nonlinear rise in tank-treading frequency is observed. Note that for Ca $\geq$ 0.8 (towards super soft particles), we observe slightly higher deviations for the NN-DNS

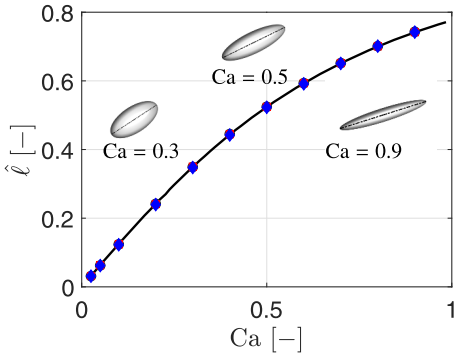

(a) Steady-state deformation parameter $\hat{\ell}$

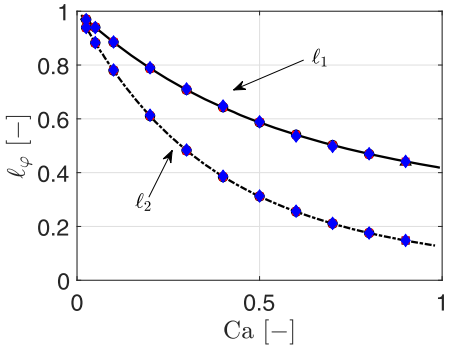

(b) Steady-state particle half axis ratios ℓ_1, ℓ_2

Fig. 11. Steady-state particle deformation parameter $\hat{\ell}$ and aspect ratios $\ell_1 = a_2/a_1$ and $\ell_2 = a_3/a_1$ as a function of the Capillary number Ca: ▬ Gao et al.,[26]. $\hat{\ell}$ and ℓ_φ, $\varphi = 1, 2$ results obtained with: ○ Roscoe's analytical expressions, ◆ present model (NN-DNS), ■ present model (NN-An.).

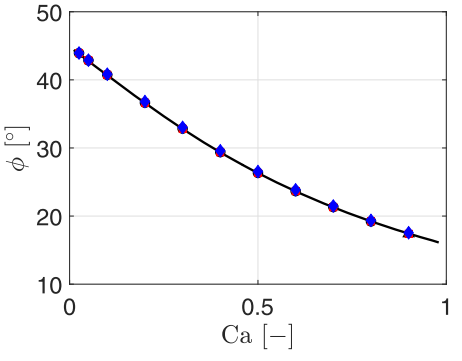

(a) Steady-state particle orientation ϕ

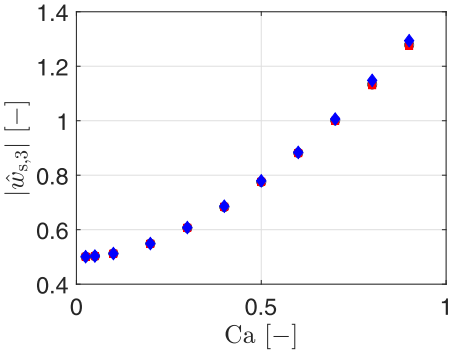

(b) Tank-treading frequency $|\hat{w}_{s\,3}| = |w_{s\,3}|/\dot{\gamma}$

Fig. 12. Steady-state particle orientation ϕ and normalised tank-treading frequency $|\hat{w}_{s\,3}| = |w_{s\,3}|/\dot{\gamma}$ as a function of the Capillary number Ca. Literature reference results: ▬ Gao et al., [26]. Results obtained with: ○ Roscoe's analytical expressions, ◆ present model (NN-DNS), ■ present model (NN-An.).

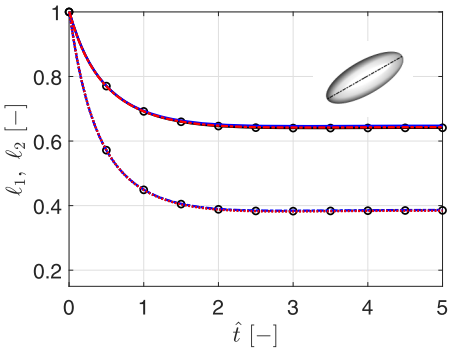

(a) Ca = 0.4: Evolution of aspect ratios $\ell_1,\ \ell_2$

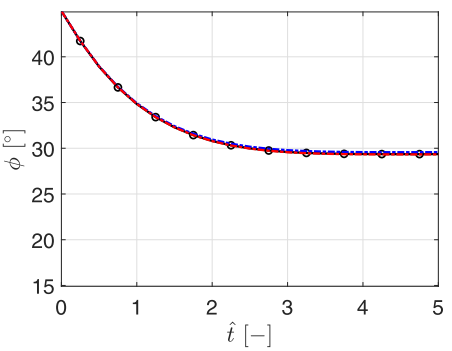

(b) Ca = 0.4: Evolution of particle orientation ϕ

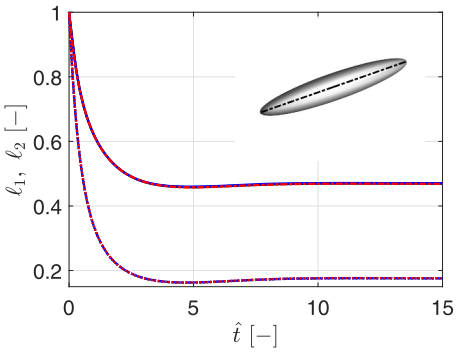

(c) Ca = 0.8: Evolution of aspect ratios $\ell_1,\ \ell_2$

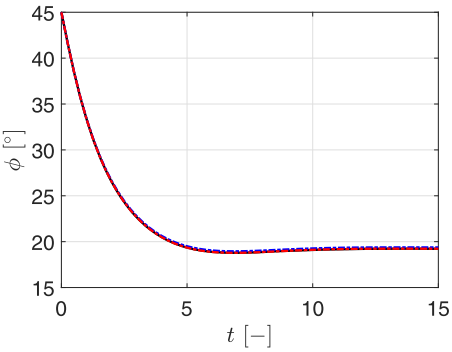

(d) Ca = 0.8: Evolution of particle orientation ϕ

Fig. 13. Transient deformation and orientation of a neo-Hookean elastic particle (Ca = 0.4) suspended in simple shear flow. Aspect ratio parameters ℓ_φ, $\varphi = 1, 2$: ○ ℓ_1/ℓ_2 Gao et al. [26], ■■ ℓ_1 / ■■ ℓ_2 present model (analytical equations), ■■ ℓ_1 / ■■ ℓ_2 present model (NN-DNS), ■■ ℓ_1 / ■■ ℓ_2 present model (NN-Analyt.). Particle orientation ϕ: ■ Gao et al. [26], ■ present model (NN-DNS), ■ present model (NN-Analyt.).

than the NN-An compared to the results obtained using Roscoe's analytical expressions. Nevertheless, both NNs demonstrate sufficient accuracy to reproduce the steady-state tank-treading frequency for all particles investigated.

5.2.2. *Transient particle deformation*

Next, we analyse the time-dependent deformation (shape and orientation) of an initially spherical elastic (neo-Hookean) particle suspended in simple shear flow. For this, we choose a particle with a Capillary number of Ca = 0.4 as investigated in the study of Gao et al., [26], and additionally a particle with Ca = 0.8. The resulting transient particle deformations are displayed in Fig. 13 (a,b) for Ca = 0.4 and in (c,d) for Ca = 0.8. Observe the excellent agreement in the aspect ratios ℓ_1, ℓ_2 as well as the particle orientation ϕ evolution between the reference results [26] and NN models in the case of Ca = 0.4. In the case of Ca = 0.8, we employ the present model using Roscoe's analytical expressions as employed in our earlier work (see Wedel [30]) as the reference, as no literature reference is available. Again, we observe an excellent agreement between the present model employing the NNs and the reference analytical model.

5.3. *Shape dynamics of soft ellipsoidal particles in simple shear flow*

Finally, we investigate the behavior of neutrally buoyant, deformable ellipsoidal particles in a simple shear flow. As demonstrated in our previous study [30] and by others [25,26], initially spherical particles suspended in such flows can evolve toward a steady state in both shape and orientation. However, this behavior does not hold for soft particles with an initially ellipsoidal shape. Prior studies [27,29] have shown that ellipsoidal particles in shear flow typically exhibit either trembling (TR) or tumbling (TU) dynamics. Trembling occurs when elastic forces, which act to preserve the initial ellipsoidal shape, dominate over hydrodynamic forces, resulting in the major axis of the deformed particle oscillating between two angular positions. In contrast, tumbling arises when hydrodynamic forces become strong enough to overcome the elastic resistance, causing the particle's major axis to undergo a full, albeit irregular, rotation. It is important to note that all material lines within the particle are continuously rotating; thus, distinguishing between TR and TU dynamics relies on visually tracking the motion of the long axis. More precisely, these regimes can be differentiated by monitoring the evolution of two material lines, l_a and l_c, which initially align with the in-plane semi-axes a_1 and a_3, respectively ($a_1 \geq a_2 \geq a_3$). Owing to ongoing internal deformation, both lines rotate in the direction defined by the solid spin tensor $\boldsymbol{w}_s$.

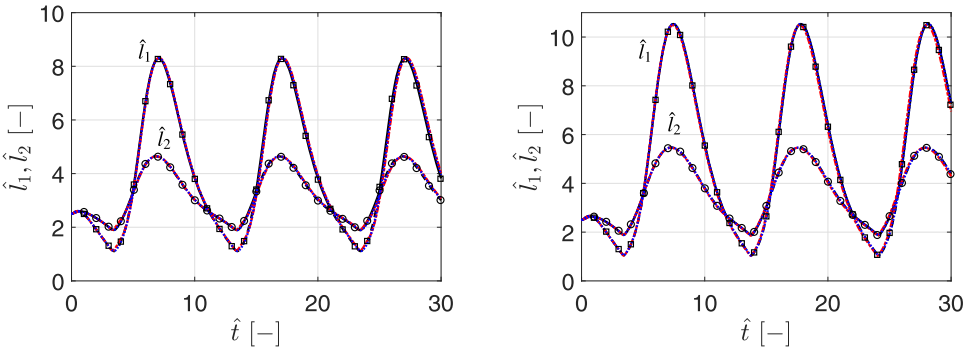

(a) Ca = 0.4 (TU) (b) Ca = 0.5 (TR)

Fig. 14. Transient deformation of a neo-Hookean elastic (initially oblate) particle with (a) Ca = 0.4 and (b) Ca = 0.5 suspended in simple shear flow. Aspect ratio parameters $\hat{\ell}_\varphi$, $\varphi = 1, 2$: Sanagavarapu et al. [29], present model (NN-An.), present model (NN-DNS).

Note that the major semi-axis a_1 and the minor semi-axis a_3 of the initial particle lie within the shear plane. In this work, we adopt the convention $a_1 \geq a_2 \geq a_3$, defining the aspect ratios as $\lambda_1 = a_1/a_3$ and $\lambda_2 = a_2/a_3$, where $\lambda_1 > \lambda_2$. In contrast, [29] defines the shape dynamics using the in-shear-plane aspect ratio $\hat{l}_1$ and the out-of-shear-plane aspect ratio $\hat{l}_2$. For the initially oblate particle considered, with its initial plane $\boldsymbol{E}'_1 - \boldsymbol{E}'_3$ lying in the shear plane $\boldsymbol{E}_1 - \boldsymbol{E}_2$, we observe that $\hat{\ell}_1(t = 0)$ initially matches $\lambda_1(t = 0)$.

The oblate particles studied have initial aspect ratios of $\hat{\ell}_1(t = 0) = \hat{\ell}_2(t = 0) = 2.5$ in and out of the shear plane. The particle softness parameter Ca is set to either 0.4 or 0.5, where the former leads to TU dynamics and the latter results in TR dynamics, as reported in [29], and reproduced in our earlier work, see [31]. Fig. 14 (a,b) displays the evolution of the in-shear and out-of-shear plane aspect ratios $\hat{\ell}_\alpha$, $\alpha = 1, 2$, for Ca = 0.4 and Ca = 0.5, respectively.

As depicted in Fig. 14 (a), both of our NN models produce results that excellently agree with the transient deformation behaviour of the initially oblate particle in the TU regime, as reported by [29]. Similarly, Fig. 14 (b) confirms that the proposed method accurately reproduces the transient deformation response of initially oblate particles in the TR regime. Furthermore, the results show that even for Ca = 0.5, where the half-axis ratio $\lambda_1 = a_1/a_3$ exceeds the upper limit of the training data set ($\lambda_1 = a_1/a_3 > 10$) at certain time instances, the model still performs sufficiently accurate and is able to reproduce the transient deformation behaviour of the ellipsoidal soft particle studied.

As illustrated in Figs. 1, 2, and 4, several form coefficients vary significantly as the particle elongation approaches $\lambda_1 = 10$. Extending the range only slightly beyond this value still falls within a regime of pronounced coefficient changes. The fact that the model is able to reproduce these variations accurately, even though it was trained only up to $\lambda_1 = 10$, highlights its robustness in capturing particle behavior slightly outside the training domain.

Remark on the efficiency of the data-driven surrogate model:

We want to point out that employing the presented surrogate model can provide a speed advantage in evaluating the tractions exerted on the particle surface, even when compared to the analytical solution, which requires evaluating elliptic integrals. This is particularly evident for triaxial particles, where the final values of α_0, β_0, and γ_0 do not degenerate to simple expressions and instead contain complete elliptic integrals of the second kind, making the analytical implementation more complex and computationally demanding depending on the employed framework. The employed NN is deliberately kept small, with two inputs, four hidden layers of 8, 8, 8, and 6 neurons, and either two outputs (shear, rotational flow) or three outputs (expansional flow), which makes inference efficient and straightforward to implement. In demonstrative evaluations, we observed that the novel surrogate model reduced the traction evaluation time of a given triaxial particle by approximately half compared to the analytical evaluation.

Finally, recall that the computational speedup of the pseudo-rigid-body approach based on analytical traction expressions relative to DNS was analyzed in our previous work (Appendix F of [30]), where a detailed discussion of efficiency is provided. There, we showed that particle-resolved simulations (BEM) require on the order of 10^2 s per particle per time step, making them impractical for large particle numbers. In contrast, our point-particle method requires only about 0.0003 s per particle per time step with analytical tractions, and about 0.00014 s with the present surrogate model, enabling simulations with millions of particles. It should also be emphasized that the surrogate framework, which here combines DNS and a neural network, is the only feasible approach in situations where analytical traction data are unavailable. This highlights the potential of the present methodology for extension to more complex soft-particle geometries, such as superellipsoids.

6. Conclusion

In this work, we present a novel data-driven surrogate framework for capturing the deformation dynamics of soft particles, both initially spherical and ellipsoidal, subjected to external flows. In the present study, the surrogate model is implemented using

neural networks. At the core of our approach is the representation of the required force dyad as a linear combination of the velocity gradient components, scaled by flow-type-dependent form coefficients. We demonstrated that such form coefficients exist and can be meaningfully defined for shear, rotational, and extensional components of the velocity gradient.

To train the NN, we investigated two complementary strategies: one utilizing analytically derived data and another relying on high-fidelity direct numerical simulation (DNS) data obtained from boundary element method (BEM) simulations. Notably, employing the NN yields a considerable computational speedup compared to direct analytical evaluation, as the latter (in general) involves the costly computation of elliptic integrals. Moreover, the use of DNS data illustrates the viability of the NN approach even in scenarios where analytical traction data is unavailable, thereby opening the door to modeling more complex geometries such as soft superellipsoidal particles.

We validated our method against established benchmarks from the literature for both initially (stress-free) spherical and ellipsoidal particles. In particular, we showed that NNs trained on either analytical or DNS data successfully captured: (i) the dynamics of ellipsoidal particles in the quasi-rigid limit within pipe flow, (ii) the steady-state and transient deformation of initially spherical particles in shear flow, and (iii) the transient deformation behavior of initially ellipsoidal particles in both the tumbling and trembling regimes. Across all cases, the NN-based models closely matched reference data, with negligible differences in accuracy between the analytically and DNS-trained networks.

Recall that, although the NN itself does not impose explicit physical constraints, the derivation of the shape factors inherently enforces properties such as symmetry and invariance. As a result, these constraints are automatically preserved in the surrogate model.

Furthermore, note that the presented surrogate model is applicable to particles over the entire range of capillary numbers considered ($0 \leq \mathrm{Ca} < 1$), as long as particle deformations remain within the training limits ($\lambda_i \leq 10$). Beyond this, the model inherits the applicability restrictions of the Jeffery-Roscoe traction framework, namely that the local flow must lie within the Stokes regime ($\mathrm{Re}_\mathrm{p} \ll 1$) and that the suspension is dilute. Importantly, the macroscopic flow field itself is not subject to restrictions on the Reynolds number. To summarize, this work brings together the strengths of the pseudo-rigid body framework, which is both efficient and versatile, and the flexibility of neural networks trained with DNS (or analytically obtained) datasets. In such cases, where analytical traction data is not available, the combination of DNS-generated training data and NN-based modeling emerges as the only feasible approach. Importantly, this maintains the computational advantages of the pseudo-rigid body model, which avoids the need for expensive surface or volume discretization typical in state-of-the-art models. As such, the proposed framework paves the way to broaden the applicability of pseudo-rigid body approaches to more realistic and complex particle geometries in flow.

Acknowledgments

The authors thank the Deutsche Forschungsgemeinschaft for the financial support in the framework of the project STE 544/75-1 and the Slovenian Research and Innovation Agency (research core funding No. P2-0196 and project J7-60118).

CRediT authorship contribution statement

Jana Wedel: Writing–original draft, Visualization, Validation, Software, Resources, Methodology, Investigation, Formal analysis, Data curation, Conceptualization; **Ivan Dominik Horvat:** Writing–review & editing, Investigation, Conceptualization; **Nejc Vovk:** Writing–review & editing, Methodology; **Matjaž Hriberšek:** Writing–review & editing, Supervision, Methodology, Formal analysis, Conceptualization; **Jure Ravnik:** Writing–review & editing, Supervision, Methodology, Formal analysis, Conceptualization; **Paul Steinmann:** Writing–review & editing, Supervision, Resources, Project administration, Methodology, Funding acquisition, Formal analysis, Conceptualization.

Data availability

Data will be made available on request.

Declaration of competing interest

The authors declare that they have no known competing financial interests or personal relationships that could have appeared to influence the work reported in this paper.

Appendix A. Pseudo-rigid body dynamics

In this section, we provide a brief overview of the pseudo-rigid body dynamics as proposed by Cohen and Muncaster [32].

Consider a solid continuum body composed of physical points P, denoted by $B = \{P\}$. Its reference configuration (here chosen as a unit sphere) is given by $\bar{\mathcal{B}}_0$, the material configuration (stress-free) by $\mathcal{B}_0$, and the spatial configuration (deformed) by $\mathcal{B}_t$. The spatial positions $\boldsymbol{x} \in \mathcal{B}_t$ of the material points P are obtained from their reference positions $\bar{\boldsymbol{X}} \in \bar{\mathcal{B}}_0$ through the deformation map $\boldsymbol{x} = \bar{\boldsymbol{y}}(t, \bar{\boldsymbol{X}})$ (a nonlinear vector-valued function of time and space). The corresponding mass densities of the solid, denoted by $\bar{\rho}_0^{\mathrm{s}}$, ρ_0^{s}, and ρ_t^{s}, are defined per unit volume in $\bar{\mathcal{B}}_0$, $\mathcal{B}_0$, and $\mathcal{B}_t$, respectively, and are scalar-valued functions of $\bar{\boldsymbol{X}}$, $\boldsymbol{X}$, and $\boldsymbol{x}$.

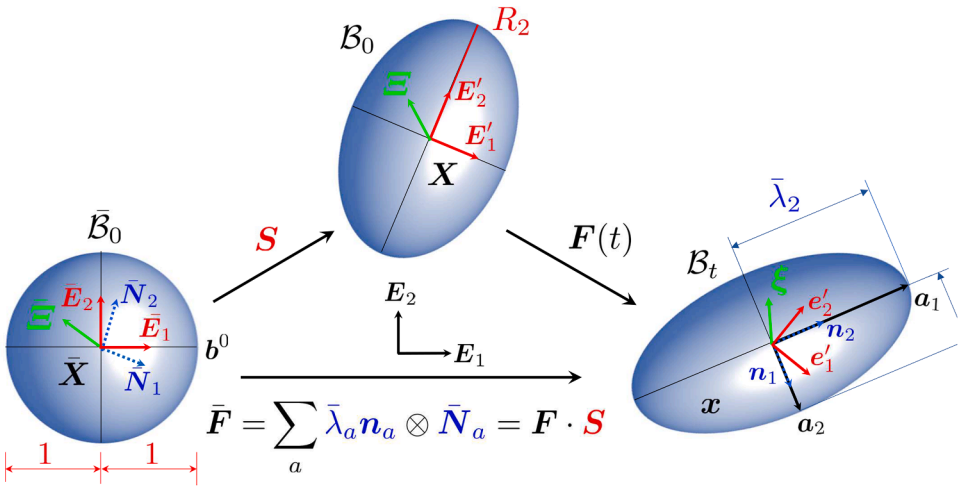

Fig. A.15. An ellipsoid undergoing affine deformation into another ellipsoid. The initial ellipsoid in the material configuration has half-axes R_a, which deform into half-axes r_a with $a = 1, 2, 3$. The relative reference, material, and spatial position vectors $\bar{\Xi}$, Ξ, and ξ connect the barycenter with the positions $\bar{X}$ in the reference configuration $\bar{\mathcal{B}}_0$, X in the material configuration $\mathcal{B}_0$, and x in the spatial configuration $\mathcal{B}_t$, respectively. The Lagrangian principal directions $\bar{N}_a$ are defined in the reference configuration $\bar{\mathcal{B}}_0$, and the Eulerian principal directions n_a in the spatial configuration $\mathcal{B}_t$, with $a = 1, 2, 3$. The fixed inertial frame of reference is denoted by E_a, $a = 1, 2, 3$ (iFoR).

The affine deformation of an ellipsoid from $\mathcal{B}_0$ (stress-free material configuration) to $\mathcal{B}_t$ (deformed spatial configuration) is sketched in Fig. A.15. Note that in this context, we employ a reference configuration $\bar{\mathcal{B}}_t$ (unit sphere) together with the shape and orientation tensor $\boldsymbol{S}$.

The material positions $\boldsymbol{X}$ of a pseudo-rigid body are expressed as

$$\boldsymbol{X} = \boldsymbol{X}_{\mathrm{c}} + \boldsymbol{\Xi} \quad \text{with} \quad \boldsymbol{\Xi} := \boldsymbol{X} - \boldsymbol{X}_{\mathrm{c}} \quad \text{and the barycenter condition} \quad \int_{\mathcal{B}_0} \rho_0^{\mathrm{s}}\, \boldsymbol{\Xi}\, \mathrm{d}V \equiv \boldsymbol{0}, \tag{A.1}$$

In Eq. (A.1), $\boldsymbol{X}_{\mathrm{c}}$ labels the material position of the barycenter, $\boldsymbol{\Xi}$ the relative material position, and $\mathrm{d}V$ the material volume element. Accordingly, the deformation map $\boldsymbol{y}(t, \boldsymbol{X})$ of a pseudo-rigid body can be expressed as a superposition of the barycenter motion $\boldsymbol{x}_{\mathrm{c}} = \boldsymbol{y}_{\mathrm{c}}(t)$ and the shape deformation $\boldsymbol{\xi}(t, \boldsymbol{\Xi})$, and takes the form

$$\boldsymbol{x} = \boldsymbol{y}(t, \boldsymbol{X}) = \boldsymbol{y}_{\mathrm{c}}(t) + \boldsymbol{\xi}(t, \boldsymbol{\Xi}) \quad \text{with} \quad \boldsymbol{X}_{\mathrm{c}} = \boldsymbol{y}_{\mathrm{c}}(t = 0) \quad \text{and} \quad \boldsymbol{\xi} := \boldsymbol{F}(t) \cdot \boldsymbol{\Xi} \quad \text{with} \quad \boldsymbol{1} = \boldsymbol{F}(t = 0), \tag{A.2}$$

where the shape change $\boldsymbol{\xi}(t, \boldsymbol{\Xi})$ is described by an affine deformation that depends on the spatially uniform deformation gradient $\boldsymbol{F}(t)$ and the relative material positions $\boldsymbol{\Xi}$, with $\boldsymbol{1}$ denoting the (two-point) unit tensor.

The spatial volume element $\mathrm{d}v$ is related to the material volume element $\mathrm{d}V$ through the Jacobian $J := \det \boldsymbol{F} > 0$, such that $\mathrm{d}v = J, \mathrm{d}V$. Since J is spatially uniform, the same relation holds for the total volumes of the pseudo-rigid body in the spatial and material configurations, i.e. $\mathrm{vol}(\mathcal{B}_t) = J, \mathrm{vol}(\mathcal{B}_0)$. To describe the velocities of the physical points P, we consider the material time derivative $\boldsymbol{v}$ of the deformation map (at fixed $\boldsymbol{X}$), which reads as

$$\boldsymbol{v} := \boldsymbol{v}_{\mathrm{c}}(t) + \boldsymbol{v}(t, \boldsymbol{\Xi}) \quad \text{with} \quad \boldsymbol{v}_{\mathrm{c}} := \dot{\boldsymbol{y}}_{\mathrm{c}}(t) \quad \text{and} \quad \boldsymbol{v} := \dot{\boldsymbol{\xi}}(t, \boldsymbol{\Xi}) = \dot{\boldsymbol{F}}(t) \cdot \boldsymbol{\Xi} =: \boldsymbol{A}(t) \cdot \boldsymbol{\Xi}\,. \tag{A.3}$$

Observe that we employ $\boldsymbol{A} := \dot{\boldsymbol{F}}$. The deformation map from the unit sphere to the material configuration contains only the affine shape-change contribution $\boldsymbol{\Xi}(\bar{\boldsymbol{\Xi}})$ and can therefore be written as

$$\boldsymbol{\Xi} := \boldsymbol{S} \cdot \bar{\boldsymbol{\Xi}} \quad \text{with} \quad \boldsymbol{S} := \sum_a R_a \boldsymbol{E}'_a \otimes \bar{\boldsymbol{E}}_a, \tag{A.4}$$

Here, R_a denote the semi-axes of the initially stress-free ellipsoidal particle in $\mathcal{B}_0$. Substituting $\boldsymbol{\Xi} := \boldsymbol{S} \cdot \bar{\boldsymbol{\Xi}}$ into Eq. (A.2), the deformation map from the unit sphere to the spatial configuration can be expressed as

$$\boldsymbol{x} = \boldsymbol{y}_{\mathrm{c}}(t) + [\boldsymbol{F}(t) \cdot \boldsymbol{S}] \cdot \bar{\boldsymbol{\Xi}}\,. \tag{A.5}$$

Appendix A.1. Barycentric dynamics

The Euler-Lagrange equation governing the barycenter dynamics of a pseudo-rigid body results as

$$\dot{\boldsymbol{v}}_{\mathrm{c}}\, m = \boldsymbol{f} \quad \text{with} \quad \boldsymbol{f} := \int_{\mathcal{B}_0} \boldsymbol{b}_0\, \mathrm{d}V + \int_{\partial\mathcal{B}_0} \boldsymbol{t}_0\, \mathrm{d}A, \tag{A.6}$$

with $\dot{\boldsymbol{v}}_c$ denoting the acceleration of the particle center and $\boldsymbol{f}$ labelling the resultant of the bulk and surface force densities $\boldsymbol{b}_0$ and $\boldsymbol{t}_0$, respectively. Furthermore, the total mass m of the pseudo-rigid body expands as

$$m := \int_{\mathcal{B}_0} \rho_0^{\mathrm{s}} \, \mathrm{d}V \, . \tag{A.7}$$

Appendix A.2. Constitutive behavior

To model the material response, we assume in the following a quasi-incompressible Neo-Hookean stored energy density $w_0 = w_0(\boldsymbol{F})$. This choice leads to the Piola stress tensor $\boldsymbol{P} = \partial w_0 / \partial \boldsymbol{F}$, which expands as

$$\boldsymbol{P} = \mu^{\mathrm{s}} \left[\boldsymbol{F} - \boldsymbol{F}^{-t} \right] + \lambda^{\mathrm{s}} \, \ln J \, \boldsymbol{F}^{-t} \, . \tag{A.8}$$

In Eq. (A.8), λ^{s} and μ^{s} denote the first and second Lamé parameters, respectively, with the limit $\lambda^{\mathrm{s}} \to \infty$ corresponding to incompressibility. The derivation connecting the pseudo-rigid body shape dynamics equation to the conventional rigid body equations of motion is presented in detail in our previous work [30].

Appendix B. Boundary element solution of Stokes flow over a particle

The Stokes flow Green's functions satisfy the incompressibility equation $\nabla \cdot \boldsymbol{u} = 0$ and are the solutions of the singularly forced Stokes equation. Defining $\boldsymbol{\xi}$ as the source point and $\hat{\boldsymbol{r}} = \boldsymbol{r} - \boldsymbol{\xi}$, a vector pointing from a field point to the source point with magnitude $r = |\hat{r}|$, the 3D free-space Green's functions can be written as:

$$\mathcal{G}_{ij} = \frac{\delta_{ij}}{\hat{r}} + \frac{\hat{r}_i \hat{r}_j}{\hat{r}^3}, \qquad \mathcal{T}_{ijk} = -6 \frac{\hat{r}_i \hat{r}_j \hat{r}_k}{\hat{r}^5}. \tag{B.1}$$

Let $\boldsymbol{t} = \boldsymbol{\sigma} \cdot \boldsymbol{n}$ denote the boundary traction, i.e., the flux of momentum into or out of the boundary. The boundary integral representation for the Stokes problem [48] is then

$$c(\boldsymbol{\xi}) u_j(\boldsymbol{\xi}) = \int_\Gamma u_i(\boldsymbol{r}) \mathcal{T}_{ijk}(\boldsymbol{r}, \boldsymbol{\xi}) n_k(\boldsymbol{r}) d\Gamma - \frac{1}{\mu^{\mathrm{f}}} \int_\Gamma \mathcal{G}_{ji}(\boldsymbol{r}, \boldsymbol{\xi}) t_i(\boldsymbol{r}) d\Gamma, \tag{B.2}$$

where $c(\boldsymbol{\xi}) = 2\alpha$ is twice the solid angle as seen from the point $\boldsymbol{\xi}$, i.e., in the interior of the domain $c = 8\pi$ and at a smooth boundary $c = 4\pi$. The normal vector $\boldsymbol{n}$ points into the domain. The first term on the right-hand side represents the double-layer potential of three-dimensional Stokes flow, and the second term is the single-layer potential of three-dimensional Stokes flow.

The boundary integral Eq. (B.2) is used as the basis of our open-source Boundary Element Method (BEM) solver (available on Zenodo [35]). The numerical implementation is based on our Laplace BEM solver [35]. We consider the boundary $\Gamma = \sum_l \Gamma_l$ to be decomposed into boundary elements Γ_l:

$$c(\boldsymbol{\xi}) u_j(\boldsymbol{\xi}) = \sum_l \int_{\Gamma_l} u_i(\boldsymbol{r}) \mathcal{T}_{ijk}(\boldsymbol{r}, \boldsymbol{\xi}) n_k^{(l)} d\Gamma - \frac{1}{\mu^{\mathrm{f}}} \sum_l \int_{\Gamma_l} \mathcal{G}_{ji}(\boldsymbol{r}, \boldsymbol{\xi}) t_i(\boldsymbol{r}) d\Gamma, \tag{B.3}$$

where $n_k^{(l)}$ is the kth component of the normal vector pointing from boundary element l into the domain.

Let Φ and Ψ be the interpolation functions used to interpolate the function and flux values within the boundary elements, i.e., $u_i = \sum_m \Phi_m u_i^{(l,m)}$ and $t_i = \sum_m \Psi_m t_i^{(l,m)}$, where $u_i^{(l,m)}$ is the mth nodal value of the function within the lth boundary element. This yields

$$c(\boldsymbol{\xi}) u_j(\boldsymbol{\xi}) = \sum_l \sum_m u_i^{(l,m)} \int_{\Gamma_l} \Phi_m \mathcal{T}_{ijk}(\boldsymbol{r}, \boldsymbol{\xi}) n_k^{(l)} d\Gamma - \frac{1}{\mu^{\mathrm{f}}} \sum_l \sum_m t_i^{(l,m)} \int_{\Gamma_l} \Psi_m \mathcal{G}_{ji}(\boldsymbol{r}, \boldsymbol{\xi}) d\Gamma. \tag{B.4}$$

The integrals above depend only on the mesh geometry and are independent of the flow solution. As such, they may be calculated in advance and stored. Since the boundary elements share nodes, the number of integrals that need to be stored is smaller than the number of integrals calculated, since the integrals, which are needed by the same node, can be summed up.

To obtain a system of equations from unknown velocities and tractions, we place the source point in all boundary nodes. Storing the integral values in matrices ($[T_{ij}]$, $[G_{ij}]$, rows corresponding to different source points, and columns to different nodes in the mesh) and flow quantities in nodal vectors $\{u_i\}$, $\{t_i\}$, we obtain the following system of equations:

$$\{u_x\}\Big[[T_{xx}] - c[I]\Big] + \{u_y\}[T_{yx}] + \{u_z\}[T_{zx}] = \frac{1}{\mu^{\mathrm{f}}}\Big[\{t_x\}[G_{xx}] + \{t_y\}[G_{xy}] + \{t_z\}[G_{xz}]\Big] \tag{B.5}$$

$$\{u_x\}[T_{xy}] + \{u_y\}\Big[[T_{yy}] - c[I]\Big] + \{u_z\}[T_{zy}] = \frac{1}{\mu^{\mathrm{f}}}\Big[\{t_x\}[G_{yx}] + \{t_y\}[G_{yy}] + \{t_z\}[G_{yz}]\Big] \tag{B.6}$$

$$\{u_x\}[T_{xz}] + \{u_y\}[T_{yz}] + \{u_z\}\Big[[T_{zz}] - c[I]\Big] = \frac{1}{\mu^{\mathrm{f}}}\Big[\{t_x\}[G_{zx}] + \{t_y\}[G_{zy}] + \{t_z\}[G_{zz}]\Big] \tag{B.7}$$

Boundary conditions include known values for $\{u_x\}$, $\{u_y\}$, $\{u_z\}$, $\{t_x\}$, $\{t_y\}$, $\{t_z\}$. Collocation points are placed only into nodes, where the value is unknown. A system of linear equations is set up for all unknowns, where in case of unknown $\{u_x\}$ or $\{t_x\}$ Eq. (B.5) is used, in case of unknown $\{u_y\}$ or $\{t_y\}$ Eq. (B.6) is used and in case of unknown $\{u_z\}$ or $\{t_z\}$ Eq. (B.7) is used. The Library of Iterative solvers for Linear Systems (LIS) (Nishida et al. [49]) is used to solve the system. Additional details of the BEM employed, such as quadrature of the integrals, can be found in [36,50,51].

When considering flow over a particle using this method, a no-slip velocity boundary condition is prescribed at the particle surface, and the algorithm renders boundary tractions. These can be integrated over the particle's surface to obtain, for example, the force and torque exerted on the particle by the fluid. The main advantage of using BEM for this task over domain-based methods, such as finite volumes, is that boundary tractions are obtained by direct solution of the system of equations and not post-processed from the velocity fields. Additionally, only the particle surface must be discretized; a volume mesh is not necessary, leading to much faster computational times.

References

[1] A. Podlozhnyuk, S. Pirker, C. Kloss, Efficient implementation of superquadric particles in discrete element method within an open-source framework, Comput. Part. Mech. 4 (2016). https://doi.org/10.1007/s40571-016-0131-6

[2] Y. You, Y. Zhao, Discrete element modelling of ellipsoidal particles using super-ellipsoids and multi-spheres: a comparative study, Powder Technol. 331 (2018) 179–191. https://doi.org/10.1016/j.powtec.2018.03.017

[3] A. Einstein, Eine neue Bestimmung der Moleküldimensionen, Ann. Phys. 324 (2) (1906) 289–306. 1011.1669v3 https://doi.org/10.1002/andp.19063240204

[4] G.K. Batchelor, J.T. Green, The determination of the bulk stress in a suspension of spherical particles to order c2, J. Fluid Mech. 56 (3) (1972) 401–427. https://doi.org/10.1017/S0022112072002435

[5] H. Brenner, et al., Rheology of a dilute suspension of axisymmetric Brownian particles, Int. J. Multiphase Flow 1 (2) (1974) 195–341. https://doi.org/10.1016/0301-9322(74)90018-4

[6] A.B. Subramaniam, M. Abkarian, L. Mahadevan, H.A. Stone, Non-spherical bubbles, Nature 438 (2005) 209–237.

[7] G.B. Jeffery, The motion of ellipsoidal particles immersed in a viscous fluid, Proc. R. Soc. London Series A, Containing Papers of a Mathematical and Physical Character 102 (715) (1922) 161–179.

[8] I.M. Krieger, Rheology of monodisperse latices, Adv. Colloid Interface Sci. 3 (2) (1972) 111–136. https://doi.org/10.1016/0001-8686(72)80001-0

[9] I. Zarraga, D. Hill, J. David, The characterization of the total stress of concentrated suspensions of noncolloidal spheres in Newtonian fluids [J. Rheol. 44, 185-220 (2000)], J. Rheol. - J RHEOL 44 (2000) 185–220. https://doi.org/10.1122/1.551083

[10] B. Snook, L.M. Davidson, J.E. Butler, O. Pouliquen, E. Guazzelli, Normal stress differences in suspensions of rigid fibres, J. Fluid Mech. 758 (2014) 486–507. https://doi.org/10.1017/jfm.2014.541

[11] P.G. Koullapis, S.C. Kassinos, M.P. Bivolarova, A.K. Melikov, Particle deposition in a realistic geometry of the human conducting airways: effects of inlet velocity profile, inhalation flowrate and electrostatic charge, J. Biomech. 49 (11) (2016) 2201–2212. https://doi.org/10.1016/j.jbiomech.2015.11.029

[12] F. Lizal, M. Cabalka, M. Maly, J. Elcner, M. Belka, E.L. Sujanska, A. Farkas, P. Starha, O. Pech, O. Misik, J. Jedelsky, M. Jicha, On the behavior of inhaled fibers in a replica of the first airway bifurcation under steady flow conditions, Aerosol Sci. Technol. 56 (4) (2022) 367–381. https://doi.org/10.1080/02786826.2022.2027334

[13] G. Bossis, J.F. Brady, Dynamic simulation of sheared suspensions. I. General method, J. Chem. Phys. 80 (1984) 5141–5154.

[14] S. Gallier, E. Lemaire, L. Lobry, F. Peters, A fictitious domain approach for the simulation of dense suspensions, J. Comput. Phys. 256 (2014) 367–387. https://doi.org/10.1016/j.jcp.2013.09.015

[15] J. Butler, B. Snook, Microstructural dynamics and rheology of suspensions of rigid fibers, Annu. Rev. Fluid Mech. 50 (2018) 299 – 318. https://doi.org/10.1146/annurev-fluid-122316-045144

[16] J. Wedel, J. and Štrakl, M. and Steinmann, P. and Hriberšek, M. and Ravnik, Can CFD establish a connection to a milder COVID-19 disease in younger people?, Comput. Mech. 67 (2021) 1497–1513. https://doi.org/10.1007/s00466-021-01988-5

[17] J. Wedel, P. Steinmann, M. Štrakl, M. Hriberšek, J. Ravnik, Risk assessment of infection by airborne droplets and aerosols at different levels of cardiovascular activity, Arch. Comput. Methods Eng. 28 (6) (2021) 4297–4316. https://doi.org/10.1007/s11831-021-09613-7

[18] J. Wedel, P. Steinmann, M. Štrakl, M. Hriberšek, Y. Cui, J. Ravnik, et al., Anatomy matters: the role of the subject-specific respiratory tract on aerosol deposition — a CFD study, Comput. Methods Appl. Mech. Eng. 401 (2022) 115372.

[19] J. Wedel, P. Steinmann, M. Štrakl, M. Hriberšek, J. Ravnik, Shape matters: Lagrangian tracking of complex nonspherical microparticles in superellipsoidal approximation, Int. J. Multiphase Flow 158 (2023) 104283. https://doi.org/10.1016/j.ijmultiphaseflow.2022.104283

[20] J. Ravnik, M. Štrakl, J. Wedel, P. Steinmann, M. Hriberšek, Stokes flow induced drag and torque on asbestos-like fibres can not be estimated by a simplistic ellipsoidal approximation, 45th International Conference on Boundary Elements and other Mesh Reduction Methods organized by WIT - Wessex Institute of Technology, U.K. (2022).

[21] H. Frohlich, R. Sack, Theory of the rheological properties of dispersions, Proc. R. Soc. London 185 (1946) 415–430.

[22] R. Cerf, On the frequency dependence of the viscosity of high polymer solutions, J. Chem. Phys. 20 (3) (1952) 395–402.

[23] J.D. Goddard, C. Miller, Nonlinear effects in the rheology of dilute suspensions, J. Fluid Mech. 28 (1967) 657–673.

[24] R. Roscoe, On the rheology of a suspension of viscoelastic spheres in a viscous liquid, J. Fluid Mech. 28 (2) (1967) 273–293.

[25] T. Gao, H.H. Hu, Deformation of elastic particles in viscous shear flow, J. Comput Phys. 228 (6) (2009) 2132–2151. https://doi.org/10.1016/j.jcp.2008.11.029

[26] T. Gao, H.H. Hu, P.P. Castañeda, Rheology of a suspension of elastic particles in a viscous shear flow, J. Fluid Mech. 687 (2011) 209–237. https://doi.org/10.1017/jfm.2011.347

[27] T. Gao, H. Hu, P. Castañeda, Shape dynamics and rheology of soft elastic particles in a shear flow, Phys. Rev. Lett. 108 (2012) 058302. https://doi.org/10.1103/PhysRevLett.108.058302

[28] T. Gao, H. Hu, P. Castañeda, Dynamics and rheology of elastic particles in an extensional flow, J. Fluid. Mech. 715 (2013) 573–596.

[29] P.K. Sanagavarapu, G. Subramanian, P.R. Nott, Shape dynamics and rheology of dilute suspensions of elastic and viscoelastic particles, J. Fluid Mech. 949 (2022) A22.

[30] J. Wedel, M. Hriberšek, J. Ravnik, P. Steinmann, A novel pseudo-rigid body approach to the non-linear dynamics of soft micro-particles in dilute viscous flow, J. Comput. Phys. 519 (2024) 113377. https://doi.org/10.1016/j.jcp.2024.113377

[31] J. Wedel, M. Hriberšek, J. Ravnik, P. Steinmann, Ellipsoidal soft micro-particles suspended in dilute viscous flow, Comput. Methods Appl. Mech. Eng. 441 (2025) 117973. https://doi.org/10.1016/j.cma.2025.117973

[32] H. Cohen, R.G. Muncaster, The Theory of Pseudo-Rigid Bodies, 33, Springer Tracts in Natural Philosophy, 1988.

[33] I. Gallily, A.H. Cohen, On the orderly nature of the motion of nonspherical aerosol particles II. Inertial collision between a spherical large droplet and axially symmetrical elongated particle, J. Colloid Interface Sci. 68 (1979) 338–356.

[34] C. Tropea, A.L. Yarin, J.F. Foss, Springer Handbook of Experimental Fluid Mechanics, Springer Berlin, Heidelberg, 2007. https://doi.org/10.1007/978-3-540-30299-5

[35] J. Ravnik, Andromeda v1.7, a BEM code, 2025, Zenodo. https://doi.org/10.5281/zenodo.14801782

[36] M. Štrakl, M. Hriberšek, J. Wedel, P. Steinmann, J. Ravnik, A model for translation and rotation resistance tensors for superellipsoidal particles in Stokes flow, J. Mar. Sci. Eng. 10 (3) (2022) 369.

[37] M. Štrakl, J. Wedel, P. Steinmann, M. Hriberšek, J. Ravnik, et al., Numerical drag and lift prediction framework for superellipsoidal particles in multiphase flows, Int. J. Comput. Methods Exp. Meas. 10 (1) (2022) 38–49. https://doi.org/10.2495/CMEM-V10-N1-38-49

[38] H.I. Andersson, F. Jiang, Forces and torques on a prolate spheroid: low-Reynolds-number and attack angle effects, Acta Mech. 230 (2) (2019) 431–447. https://doi.org/10.1007/s00707-018-2325-x

[39] J. Ravnik, C. Marchioli, A. Soldati, Application limits of Jeffery's theory for elongated particle torques in turbulence: a DNS assessment, Acta Mech. 229 (2) (2018) 827–839. https://doi.org/10.1007/s00707-017-2002-5

[40] C. Runge, Über empirische Funktionen und die interpolation zwischen äquidistanten ordinaten, Z. Math. Phys. 46 (1901) 224–243.
[41] C.M. Bishop, Pattern Recognition and Machine Learning, Springer, New York, New York, 2006.
[42] K. Hornik, M. Stinchcombe, H. White, Multilayer feedforward networks are universal approximators, Neural Netw. 2 (5) (1989) 359–366. https://doi.org/10.1016/0893-6080(89)90020-8
[43] I. Goodfellow, Y. Bengio, A. Courville, Deep Learning, MIT Press, 2016. http://www.deeplearningbook.org.
[44] A. Seyed-Ahmadi, A. Wachs, Physics-inspired architecture for neural network modeling of forces and torques in particle-laden flows, Comput. Fluids 238 (2022) 105379. https://doi.org/10.1016/j.compfluid.2022.105379
[45] H.A. Stone, Dynamics of drop deformation and breakup in viscous flows, Annu. Rev. Fluid Mech. 26 (1994) 65–102.
[46] L. Tian, G. Ahmadi, Z. Wang, P.K. Hopke, et al., Transport and deposition of ellipsoidal fibers in low Reynolds number flows, J. Aerosol. Sci. 45 (2012) 1–18.
[47] R. Gerum, E. Mirzahossein, M. Eroles, J. Elsterer, A. Mainka, A. Bauer, S. Sonntag, A. Winterl, J. Bartl, L. Fischer, S. Abuhattum, R. Goswami, S. Girardo, J. Guck, S. Schrüfer, N. Ströhlein, M. Nosratlo, H. Herrmann, D. Schultheis, F. Rico, S.J. Müller, S. Gekle, B. Fabry, Viscoelastic properties of suspended cells measured with shear flow deformation cytometry, eLife 11 (2022) e78823. https://doi.org/10.7554/eLife.78823
[48] C. Pozrikidis, A Practical Guide to Boundary Element Methods with the Software Library BEMLIB, CRC Press, 2002.
[49] A. Nishida, Experience in developing an open source scalable software infrastructure in Japan, in: D. Hutchison, T. Kanade, J. Kittler, J.M. Kleinberg, F. Mattern, J.C. Mitchell, M. Naor, O. Nierstrasz, C. Pandu Rangan, B. Steffen, M. Sudan, D. Terzopoulos, D. Tygar, M.Y. Vardi, G. Weikum, D. Taniar, O. Gervasi, B. Murgante, E. Pardede, B.O. Apduhan (Eds.), Computational Science and Its Applications – ICCSA 2010, 6017, Springer Berlin Heidelberg, Berlin, Heidelberg, 2010, pp. 448–462.
[50] A. Šušnjara, O. Verhnjak, D. Poljak, M. Cvetković, J. Ravnik, Stochastic-deterministic boundary element modelling of transcranial electric stimulation using a three layer head model, Eng. Anal. Bound. Elem. 123 (2021) 70–83. https://doi.org/10.1016/j.enganabound.2020.11.010
[51] A. Šušnjara, O. Verhnjak, D. Poljak, M. Cvetković, J. Ravnik, Uncertainty quantification and sensitivity analysis of transcranial electric stimulation for 9-subdomain human head model, Eng. Anal. Bound. Elem. 135 (2022) 1–11. https://doi.org/10.1016/j.enganabound.2021.10.026